GFZ

Helmholtz-Zentrum

POTSDAM

Originally published as:

High-frequency seismic radiation from Maule earthquake (M_w 8.8, 2010 February 27) inferred from high-resolution backprojection analysis

M. Palo,[1] F. Tilmann,[1,2] F. Krüger,[3] L. Ehlert[3] and D. Lange[4]

[1]*Helmholtz-Zentrum Potsdam, Deutsches GeoForschungsZentrum GFZ, Potsdam, Germany. E-mail: mpalo@gfz-potsdam.de*
[2]*Freie Universität Berlin, Fachrichtung Geophysik, Berlin, Germany*
[3]*Universität Potsdam, Institut für Erd- und Umweltwissenschaften, Potsdam, Germany*
[4]*GEOMAR Helmholtzzentrum für Ozeanforschung, Kiel, Germany*

SUMMARY

The Maule earthquake (2010 February 27, M_w 8.8, Chile) broke the subduction megathrust along a previously locked segment. Based on an international aftershock deployment, catalogues of precisely located aftershocks have become available. Using 23 well-located aftershocks, we calibrate the classic teleseismic backprojection procedure to map the high-frequency seismic radiation emitted during the earthquake. The calibration corrects traveltimes in a standard earth model both with a static term specific to each station, and a 'dynamic' term specific to each combination of grid point and station. The second term has been interpolated over the whole slipping area by kriging, and is about an order of magnitude smaller than the static term. This procedure ensures that the teleseismic images of rupture development are properly located with respect to aftershocks recorded with local networks and does not depend on accurate hypocentre location of the main shock.

We track a bilateral rupture propagation lasting ∼160 s, with its dominant branch rupturing northeastwards at about 3 km s⁻¹. The area of maximum energy emission is offset from the maximum coseismic slip but matches the zone where most plate interface aftershocks occur. Along dip, energy is preferentially released from two disconnected interface belts, and a distinct jump from the shallower belt to the deeper one is visible after about 20 s from the onset. However, both belts keep on being active until the end of the rupture. These belts approximately match the position of the interface aftershocks, which are split into two clusters of events at different depths, thus suggesting the existence of a repeated transition from stick-slip to creeping frictional regime.

Key words: Earthquake source observations; Wave propagation; Subduction zone processes.

1 INTRODUCTION

During megathrust earthquakes, the rupture front can propagate for distances of several hundred kilometres, following irregular patterns on the fault reflecting site-dependent frictional properties or topographic irregularities. In recent years, the time-evolution of the rupture process during mega-earthquakes has been inferred by following the coherent seismic radiation released during the main event and detected in the far field, thus providing a powerful and very efficient method for tracking the rupture front, with applications also in near real-time monitoring (Ammon *et al.* 2005; Ishii *et al.* 2005; Krüger & Ohrnberger 2005; Rössler *et al.* 2010; Meng *et al.* 2011).

In this approach, the seismic wave front recorded by an array of sensors at teleseismic distances is projected back onto the source region, allowing recovery of the time-evolution of the source position of the seismic radiation during large earthquakes. Starting from a 2-D grid of potential source positions in the rupture area and a velocity model, seismic traces are time-shifted and a function measuring the degree of coherence of the stack of shifted waveforms is calculated. The instantaneous source position is estimated as the gridpoint providing the highest coherence among the traces. The traveltimes used for time-shifting are usually calculated by adding the theoretical traveltime in a 1-D global velocity model to receiver-dependent time corrections, which are supposed to account for lateral velocity variations.

The time corrections are generally calibrated at the hypocentre and inferred in an empirical way. Specifically, the receiver-dependent correction terms (station terms) are estimated by cross-correlating the first few seconds at the onset of the main shock and comparing the observed time-shifts with the predicted traveltimes based on the catalogue hypocentre and a 1-D model (Ishii *et al.* 2005). The hypocentre-calibrated (HC, hereafter) approach

implicitly assumes that the time corrections do not change over the entire rupture area, which is not necessarily satisfied for the huge rupture areas of great megathrust events. Instead, the corrections to the traveltimes might depend on the specific source–receiver path, and thus path-dependent time corrections should be taken into account together with the receiver-dependent corrections in order to correct for these velocity variations. Also, this approach implies that any error in the catalogue hypocentre will cause a systematic shift of the inferred rupture history; for example, the difference between various estimated hypocentres for the Maule earthquake was nearly 50 km (Vigny *et al.* 2011). Ishii *et al.* (2007) thus substituted receiver-dependent corrections with path-dependent corrections, which were calibrated by measuring interstation time shifts for several aftershocks; afterwards, they extended these corrections to a grid of the source area by weighting them with the inverse of the distance between the aftershocks and the gridpoints. This results in matching the shifts from the aftershocks exactly where the aftershock is occupying a grid cell. Any error in the time-shift measurement of individual aftershocks will thus not average out, maybe resulting in the apparent expulsion of recovered energy release by some of the aftershocks (see figs 3 and 5 of Ishii *et al.* 2007).

In this paper, we will introduce a different approach in which receiver-dependent and path-dependent corrections are considered separately, and the total traveltimes are the sum of the times predicted for a 1-D global velocity model, the receiver-dependent corrections and the path-dependent corrections. Throughout the paper, we will refer to the receiver-dependent correction as the static correction, and to the path-dependent correction as the dynamic correction. Moreover, we will estimate the static correction by averaging the mean time shifts between sensors relative to a set of aftershocks covering the source area. For most of the events in this set, high precision locations are available either from a local aftershock study (Lange *et al.* 2012), or from earthquakes relocated using double-difference techniques on teleseismic and local recordings (Pesicek *et al.* 2012). The procedure is thus independent of the catalogue hypocentre itself, which allows a detailed interpretation of the relative positions of high frequency seismic radiation and aftershock distribution. Finally, we extend the dynamic corrections to the entire source area by kriging, a spatial interpolation method (Cressie 1993).

Our approach is applied to the M_w 8.8 Maule earthquake (2010 February 27), which ruptured a ∼500 km segment of the convergent margin between the Nazca and South America plates. Exploiting the finer resolution of the estimated emission areas, we will process very high frequency bands (up to 2–8 Hz), which are potentially able to enlighten small scale properties of the rupture front. Specifically, we will reconstruct the path of the energy emission during the rupture. It has to be remembered that at high frequencies seismic wave radiation is not controlled by the magnitude of the overall slip, but by changes in either rupture velocity or slip along the rupture (e.g. Yagi *et al.* 2012). In this sense mapping the high-frequency radiation can be thought of as shedding light on the roughness of the fracturing interface as well as indicating the actual begin and end of the rupture, which are associated with strong accelerations and decelerations, and thus with high frequency seismic radiation.

2 MAULE EARTHQUAKE

The Maule earthquake nucleated in Central Chile on 2010 February 27 on the megathrust boundary between the Nazca and the South America plates, filling (at least partially) the seismic gap (Moreno
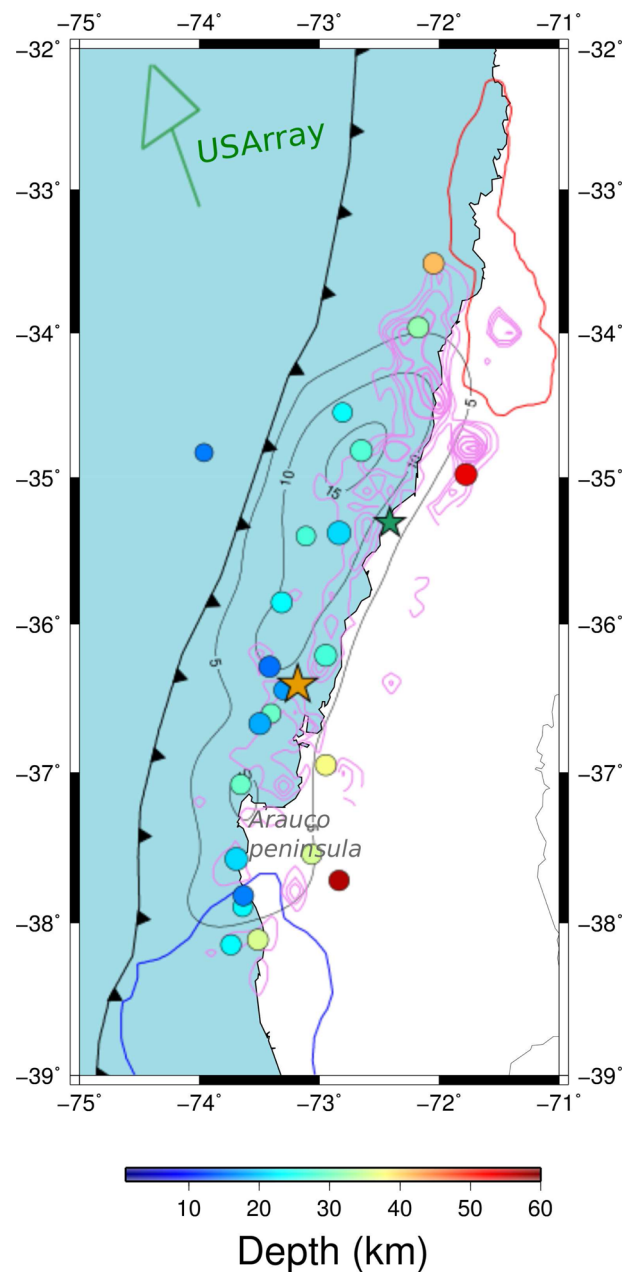

Figure 1. Epicentres of aftershocks used to compute traveltimes. Size of the dots is proportional to the magnitude. Colours display the hypocentre depth. The black contours display the coseismic slip (Moreno *et al.* 2012), while the violet contours define the aftershock density (Lange *et al.* 2012). The direction of the array of seismometers adopted is indicated by the green arrow. Red and blue lines enclose 5-m and 1-m coseismic areas of the 1960 (Moreno *et al.* 2009) and 1985 (Barrientos 1988) events, respectively. The yellow star marks the epicentre of the Maule earthquake as relocated by Vigny *et al.* (2011), and the green star marks the epicentre of the M_w 7.0 event of 2012 March 25 (Ruiz *et al.* 2013).

et al. 2012) in the segment last activated during the great event of 1835 documented by Charles Darwin (Darwin *et al.* 1895, Fig. 1). At the time of writing, the Maule earthquake is the sixth largest event recorded in instrumental times and a large amount of geophysical data are available in particular for the post-seismic phase, including land and ocean-bottom seismic recordings and continuous and campaign-mode geodetic observations (Hicks *et al.* 2012; Lange *et al.* 2012; Bedford *et al.* 2013; Lin *et al.* 2013).

The earthquake nucleated at 36.4°S, 73.2°W at a depth of about 35 km and propagated bilaterally (e.g. Vigny *et al.* 2011), possibly favoured by a subducted topographic high, which could act as a point of stress accumulation and as a barrier to rupture propagation (Hicks *et al.* 2012). The coseismic slip pattern displays two major peaks with most of the slip falling in the northern patch (Lorito *et al.* 2011; Pollitz *et al.* 2011; Vigny *et al.* 2011; Moreno *et al.* 2012; Lin *et al.* 2013, Fig. 1). The main patch (slip ∼15–20 m) is concentrated north/northeast of the epicentre in an area extending northwards up to 34°S, roughly bounded by the rupture zone of the earthquake of 1985 March 3 (M_w 8.2). A secondary patch (∼5–10 m) is located south/southwest of the epicentre and is less extended than the former. Its southern tip falls at about 38°S (Arauco peninsula), near the northern edge of the megathrust earthquake of 1960 May 22 (M_w 9.5), partially overlapping the area of its foreshocks (up to $M_w = 8.1$ Cifuentes 1989). Arauco peninsula has been suggested to act as a barrier for rupture propagation for both the 1960 and 2010 earthquakes (e.g. Moreno *et al.* 2012; Lin *et al.* 2013) and possibly many earlier earthquakes (Melnick *et al.* 2009). In the downdip direction, the rupture area extends to about 160 km from the trench.

Aftershock seismicity on the subduction interface is mostly located at the downdip side of the coseismic slip area, with the vast majority of the events located along the northern coseismic slip patch but extending up to ∼50 km beyond the northern edge of this patch (Lange *et al.* 2012; Rietbrock *et al.* 2012; Hayes *et al.* 2013). Moreover, differently from the coseismic slip pattern, no obvious interruption in the aftershock distribution is visible in the epicentral area; there is a local maximum just north of the epicentre but this still corresponds to a much lower event density than the area to the northeast of the main slip patch (fig. 1 and Lange *et al.* 2012).

The depth distribution of the plate interface seismicity displays a peculiar pattern, being mostly split into two spatially separated groups. The principal group is located at about 100 km from the trench at a depth of 25–35 km. The secondary group is located at a depth of 40–50 km at a distance from the trench of about 150 km, leaving a 20–30 km wide gap with sparse or absent interface seismicity (Lange *et al.* 2012; Rietbrock *et al.* 2012). In both groups shallowly dipping thrust events dominate. The deeper group falls well beyond the downdip edge of the geodetically inferred coseismic slip area and overlaps with the post-seismic slip area, which in turn is concentrated at the downdip edge of the co-seismic slip pattern, with two minor patches at its northern and southern ends (Bedford *et al.* 2013; Lin *et al.* 2013).

Previous backprojection studies revealed a dominant northward rupture propagation (Kiser & Ishii 2011; Wang & Mori 2011; Koper *et al.* 2012). The location of peak energy radiation along both strike and dip appears to be dependent on the analysed frequency. Indeed, low-frequency (<0.1 Hz) energy is emitted in the shallow part of the subduction interface located just north/northeast of the epicentre, whereas higher frequencies are mostly emitted in the northern part of the rupture area in a deeper zone (Wang & Mori 2011; Koper *et al.* 2012). In particular, at high frequencies (1–5 Hz) a jump in the northward migration of the rupture front is observed around 35.5°S, with a consequent subdivision of the rupture into two main segments with regular propagation speed elongated approximately parallel to the coastline, extending from the epicentre to about 35.7°S and from 35.1°S to about 33.9°S (Kiser & Ishii 2011), and apparently much faster propagation in the jump region with much reduced emission of seismic radiation. Kiser & Ishii (2013) propose that the gap left by this jump of the radiation has been filled by the 2012 March 25 aftershock (M_w 7.1).

3 METHOD

In the backprojection analysis, the spatial coherence of a seismic phase is measured by stacking the seismograms of stations located at teleseismic distances (Ishii *et al.* 2005; Krüger & Ohrnberger 2005). The potential source positions are searched on a grid and seismograms are time-shifted according to the predicted traveltimes between the stations and the gridpoints, as in classic beamforming (e.g. Rost & Thomas 2002). For actual emission points the seismograms will overlap and result in constructive interference; the grid point corresponding to the highest value of the stack can be considered the most probable or dominant source position. At a first stage, a 1-D global velocity model is used to infer the time shifts. Formally, the function to be maximized is the beam power:

$$E_i(t) = \int_0^L \left| \sum_{k=1}^N u_k(t + t_{ik} + \tau) \right|^2 d\tau, \qquad (1)$$

where *i* enumerates the points of the source grid, u_k is the seismogram of the *k*th station, t_{ik} is the traveltime between the *i*th source grid node and the *k*th station in the reference model, *N* is the number of stations, *L* is the length of the time window. *L* must be chosen sufficiently long to encompass at least three to four oscillations of the dominant period. The time integration is accomplished by a summation for sampled data. To make the formulas more concise, the integration limits will be omitted for the remainder of the method description, but are implied throughout.

For real data, 3-D heterogeneity can cause source–station pairs having equal distances to be associated with different traveltimes. For that reason, a static time correction was introduced by Ishii *et al.* (2005, 2007)

$$E_i(t) = \int \left| \sum_{k=1}^N u_k(t + t_{ik} + \Delta t_k + \tau) \right|^2 d\tau, \qquad (2)$$

where Δt_k is the time correction to the 1-D velocity model at each station (static correction). This term largely absorbs heterogeneity below the receiver array and is often estimated from the time shifts of the first few seconds of the main shock relative to the times predicted for the catalogue hypocentre. However, in the case of very large source area, such as those involved in great earthquakes, travel time anomalies might vary with the source position. Therefore, another correction to the traveltimes is needed:

$$E_i(t) = \int \left| \sum_{k=1}^N u_k(t + t_{ik} + \Delta t_k + \delta t_{ik} + \tau) \right|^2 d\tau$$

$$= \int \left| \sum_{k=1}^N u_k(t'_{ik} + \tau) \right|^2 d\tau, \qquad (3)$$

where δt_{ik} is the time correction associated with the path between the *i*th source grid point and the *k*th station. $t'_{ik} = t + t_{ik} + \Delta t_k + \delta t_{ik}$ is the predicted arrival time including all correction terms, defined for convenience.

In this paper, besides the classical beam power, we adopt a normalized version of the stacking function, that is the semblance (*S*), which is the power of the stacked traces normalized with the total power in the seismograms (Neidell & Taner 1971; Rössler *et al.* 2010). Semblance is a measure of the fraction of the radiated energy released as coherent waves and it has a better resolution than the classical beam power for low-energy radiation (Neidell & Taner 1971). In fact, due to the normalization, semblance is not sensitive to pure amplitude effects such as those induced by station site struc-

tures and directivity. S ranges in the interval $[0 - 1]$, with $S = 1$ corresponding to perfectly coherent signals, and has an expectation value of $1/N$ for uncorrelated white noise:

$$S_i(t) = \frac{1}{N} \frac{\int \left| \sum_{k=1}^{N} u_k(t' + \tau) \right|^2 d\tau}{\int \sum_{k=1}^{N} u_k^2(t' + \tau) d\tau} \tag{4}$$

While S is a good estimate of the spatial coherence of the seismic radiation and is strongly sensitive to the alignment of the individual traces but does not contain information on its amplitude, E gives an estimate of the radiated energy in the analysed frequency band but energetic portions of the rupture tend to dominate over periods with relatively weaker seismic radiation, exacerbating the swimming artefact (Ishii *et al.* 2007; Koper *et al.* 2012).

In that sense, S and E must be considered complementary and they will be both computed throughout the paper. S can be reduced by interference from multiple sources acting simultaneously, such as for example during bilateral rupture propagation. However, if the sources are clearly separated in space, they can still be identified as separate local maxima in the semblance maps.

In this study, we calculate semblance and energy of the P phase in three frequency bands: 0.4–3 Hz, 1–4 Hz, 2–8 Hz. The spectral content of the main shock is shown in Fig. 2(b). Signal amplitudes exceed noise amplitudes until at least 6 Hz and possibly up to 10 Hz. Because of the spectral decay at high frequencies, the seismograms at each bandpass are dominated by the lower frequencies, but the higher frequencies can still contribute to the resolution of the back-projection method. Notably, the 2–8 Hz filtered seismogram still has a very large signal-to-noise ratio despite absolute amplitudes an order of magnitude smaller than for the 1–4 Hz seismogram; it also has a noticeably higher frequency content than the 1–4 Hz seismogram, so the energy is not dominated by lower frequencies leaking through the lower flank of the bandpass filter response.

We calculate semblance and energy in time windows of $L = 10$, 8, 4 s for the three frequency bands, respectively, employing a time step of 2 s. In detail, for each time window we estimate S_i and E_i and look at the distribution in time and space of the seismic radiation in order to define principal and secondary sources and their time-evolution. The gridpoints in the source area range between 32°S and 39°S in latitude and between 69°W and 76°W in longitude, with a grid spacing of 0.1°, except for the 2–8 Hz frequency band, for which the spacing is 0.05°.

S_i and E_i depend on three parameters: traveltimes based on a 1-D velocity model t_{ik}, station (static) time correction Δt_k and path (dynamic) time correction δt_{ik}. The t_{ik} are computed using the ak135 model (Kennett *et al.* 1995), whereas the other two corrections are estimated by a two-step process based on the time delays measured from a set of calibration aftershocks.

We select aftershocks with magnitudes $m_b \geq 5.1$ and thrust focal mechanisms (when known), covering the slip area as homogeneously as possible. After a visual inspection and a preliminary cross-correlation analysis, the events with insufficient signal-to-noise ratio or waveform similarity were rejected. The selected events are listed in Table 1 and plotted in Fig. 1. We process the traces of these events recorded by seismic broad-band stations located in the United States (hereafter USArray, see map in Figs 3 and 4). Most stations belong to the Transportable Array, a very dense seismic network (mean spacing 70 km) moving across the United States. The data are sampled at a frequency of 20 Hz or higher. The instrument response is removed in order to obtain vertical ground velocity time series, which are then bandpass filtered between 0.4

and 3 Hz. Relative time shifts between the stations are computed by cross-correlating the first 5–12 s of the waveforms (Fig. 5).

For each event j ($j = 1, \ldots, M$, with M number of events), we estimate the relative shifts between all possible pairs of stations (with respect to the traveltime predicted by 1-D model) by maximizing their cross-correlation functions. In this way, we get two $N \times N$ (with N number of stations) matrices: the matrix of the cross-correlation coefficients and the matrix of the time-shifts. Then, we compute the mean value of the cross-correlation coefficients and of the relative time shifts associated with each station, and select only those stations whose mean cross-correlation is higher than a threshold. Such a threshold depends on the event and is chosen in a way that the waveforms of the selected stations shifted by the corresponding mean time-shifts are well aligned and still clearly coherent with each other. This threshold is normally in the range 0.5–0.7 (see Fig. 5). The relative time delays are the averages of the relative time-shifts of the remaining stations. The process is repeated for all the events. In this way, we get a set of mean relative delays (hereafter, $\mathbb{S}_1, \ldots, \mathbb{S}_M$) associated with a set of stations for all events. We remark that $\mathbb{S}_j$ and $\mathbb{S}_k$ with $j \neq k$ may share only a subset of stations. In our case, the number of stations ranges between 402 and 81.

Starting from these sets $\mathbb{S}_j$ ($j = 1, \ldots, M$), we calculate the two time corrections introduced in eq. (3). As already outlined, we perform a two-step process, in which at first we process the $\mathbb{S}_j$, removing from them the effects of different source and station positions and thus making them mutually consistent. In detail, we sort $\mathbb{S}_j$ by the number of stations in a way that $\mathbb{S}_1$ has the largest set of stations, and $\mathbb{S}_M$ has the smallest one. Then, we estimate the mean difference between time shifts of common stations of $\mathbb{S}_1$ and $\mathbb{S}_2$, and subtract this difference from $\mathbb{S}_2$. This takes into account the difference in mean delay resulting from the fact that both sets include a different collection of stations. In this way, we get $\mathbb{S}_2'$. To get $\mathbb{S}_3'$, we average the contribution of the mean difference between time shifts of common stations of two pairs of events: $\mathbb{S}_1$–$\mathbb{S}_3$ and $\mathbb{S}_2'$–$\mathbb{S}_3$. For the jth event, the contribution from the $j - 1$ pairs $\mathbb{S}_l$–$\mathbb{S}_j$ (with $l = 1, \ldots, j - 1$) are averaged. Finally, we get M new sets (hereafter, $\mathbb{S}_j'$, with $j = 1, \ldots, M$).

We now calculate from all the $\mathbb{S}_j'$ the mean time shift for each station, which represents the static correction Δt_k of eq. (3). Then, we remove Δt_k from $\mathbb{S}_j'$, thus getting new sets of time delays (hereafter, $\mathbb{S}_j''$, $j = 1, \ldots, M$). These new sets only contain the effects on time delays of different paths, as all delays for a station average to zero (as we have subtracted the averages in the previous step). $\mathbb{S}_1'', \ldots, \mathbb{S}_M''$ constitute the third (dynamic) correction (δt_{ik}) of eq. (3), available for source locations coincident with calibration aftershock locations. We remark that whereas the static correction reflects the overall velocity discrepancies with the 1-D model along all the paths connecting the source area and one station, thus typically being representative of the structure below the station, the dynamic correction is expected to be mostly affected by velocity heterogeneities in the source area and along the propagation path.

The second step consists of estimating the δt_{ik} values for the whole potential source area starting from the sets $\mathbb{S}_j''$ by kriging, a robust spatial interpolation method well established in geoscience and suitable for data sets with non-uniform spatial sampling (Cressie 1993; Trauth *et al.* 2010). Kriging takes into account spatial correlations between the variables to be estimated such that measurements very close to each other are effectively simply averaged, while the influence of more distant points is reduced. The characteristic function describing the statistical properties of the parameter of interest is estimated from the data themselves (see
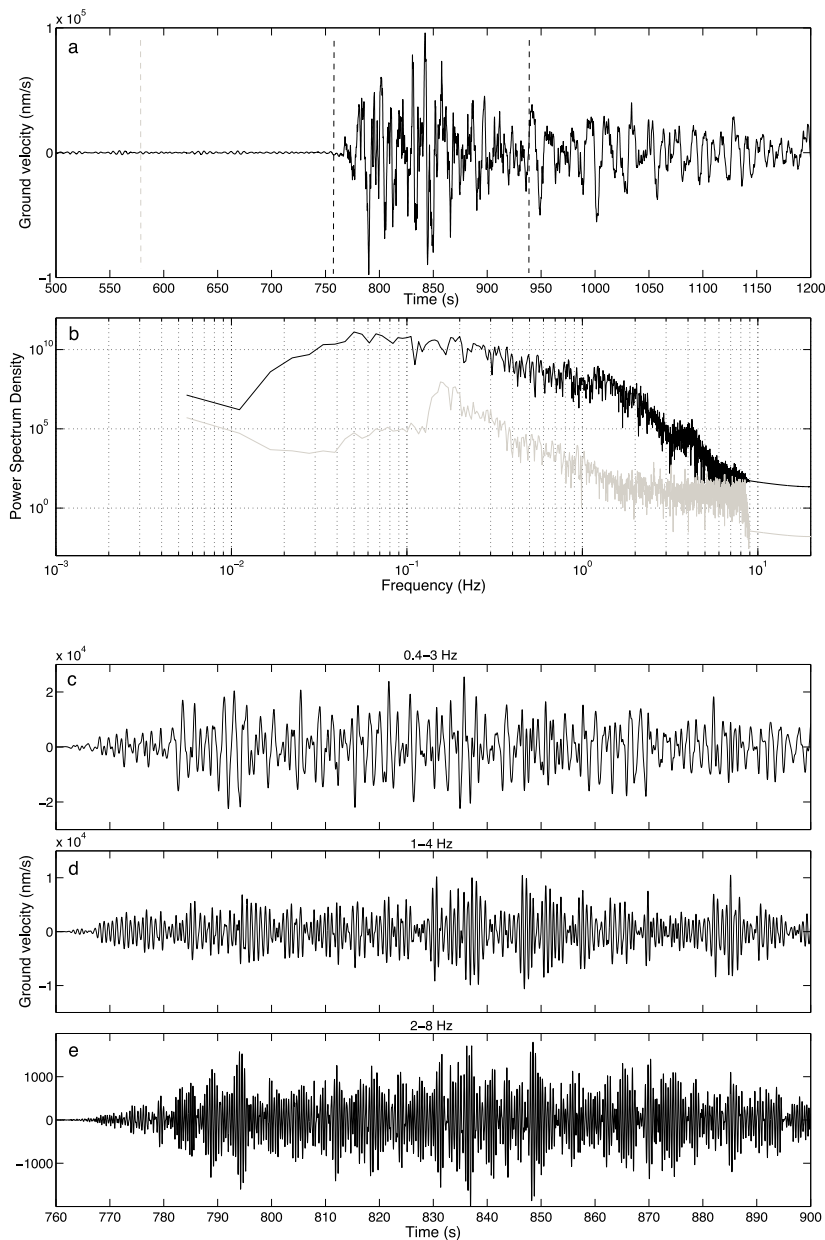
Figure 2. (a) Vertical component broadband waveforms of the main shock at station A30A (48.94° N 98.30° W – Transportable Array). Zero on the time scale marks the origin time of the main shock. (b) Power spectral density (PSD) of the first three minutes (analysis window enclosed between the black vertical dotted lines in a) in black. Grey line shows noise PSD in the immediately preceding time window. (c–e) Bandpass filtered seismograms of the first few minutes of the main shock rupture in the frequency bands for which backprojection analysis was carried out.

appendix for a short description of the kriging approach as applied here).

In our case, $\mathbb{S}''_j (j = 1, \ldots, M)$ is the process sampled at the epicentres, and we estimate the interpolated path time shifts $\mathbb{S}''_{krig}$ in the grid in the source area described above. $\mathbb{S}''_{krig}$ is an estimate of the dynamic corrections δt_{ik} over the entire source area; the process is applied for each station k separately. The kriging procedure adjusts the weights of the delays from the different earthquakes in order to minimize the standard error of the interpolated value rather than using any *a priori* fixed weighing scheme. Moreover, separating the dynamic and static parts makes the interpolation process more robust compared to using the complete traveltime anomaly relative to a 1-D model.

The final traveltimes adopted for backprojection analysis will be the sum of the three contributions of eq. (3) (t_{ik}, Δt_k, δt_{ik}), in which the traveltimes predicted from the 1-D model (t_{ik}) have been inferred adopting a constant depth of 30 km, which is broadly consistent with the mean depth of the part of the slab activated during the mainshock. However, the process is hardly sensitive to the assumed depth and velocity model as any deviations would be absorbed into the correction terms.

3.1 Results of calibration procedure

Fig. 3 displays the static corrections. A sharp separation between fast and slow regions is visible. Specifically, a slow area is mostly

Table 1. Origin time, epicentre and magnitude of the aftershocks used for calibrating the static and dynamic corrections. Sources for earthquakes: 1 – Pesicek *et al.* (2012), 2 – Lange *et al.* (2012), 3 – NEIC catalogue. (2) is a local catalogue based on the IMAD aftershock deployment and (1) is a catalogue based on a combination of teleseismic picks and the local picks for selected events in cat. (2) [indicated by 1,2 in the table—the final location was taken from (1)]. Earthquakes pre- or postdating the deployment were relocated relative to those with local picks (marked by 1 only in table). Magnitude is m_b for catalogue 1 and M_w for catalogues 2 and 3.

Label	Date	Latitude (°)	Longitude (°)	Depth (km)	Magnitude	Catalogue
1	2010-02-27 07:12:27.41	−33.96	−72.17	32.0	6.0	1
2	2010-02-27 07:37:17.90	−36.95	−72.94	37.4	6.0	1
3	2010-02-27 08:25:28.12	−34.82	−72.65	27.9	6.1	1
4	2010-02-27 19:00:07.68	−33.52	−72.05	41.6	5.9	1
5	2010-02-27 23:02:03.18	−37.72	−72.84	57.0	5.8	1
6	2010-02-28 11:25:36.23	−34.98	−71.78	53.7	6.2	1
7	2010-03-02 06:10:51.29	−34.55	−72.81	23.3	5.5	1
8	2010-03-03 17:44:26.04	−36.60	−73.40	29.3	5.6	1
9	2010-03-05 11:47:06.68	−36.67	−73.50	18.2	6.1	1
10	2010-03-15 11:08:29.00	−35.85	−73.31	23.0	5.9	1
11	2010-03-16 02:21:57.22	−36.29	−73.41	14.9	6.0	1
12	2010-03-21 18:31:01.60	−36.45	−73.30	17.5	5.6	1,2
13	2010-03-23 03:44:55.74	−34.83	−73.96	15.5	5.1	1,2
14	2010-03-28 21:38:30.70	−35.40	−73.11	27.3	5.5	1,2
15	2010-04-02 22:58:07.80	−36.21	−72.94	27.2	6.1	1,2
16	2010-04-23 10:03:05.10	−37.55	−73.06	35.5	5.8	1,2
17	2010-05-03 23:09:41.80	−38.15	−73.74	23.1	5.8	1,2
18	2010-06-29 01:40:00.20	−37.90	−73.64	22.9	5.6	2
19	2010-07-14 08:32:22.71	−38.11	−73.51	35.7	5.9	1,2
20	2010-09-09 07:27:58.90	−37.08	−73.65	29.3	5.8	1,2
21	2010-10-23 05:58:27.73	−37.82	−73.64	15.8	5.7	1
22	2011-02-14 03:40:15.20	−35.38	−72.83	12	6.7	3
23	2011-06-01 12:55:25.40	−37.58	−73.70	12	6.3	3

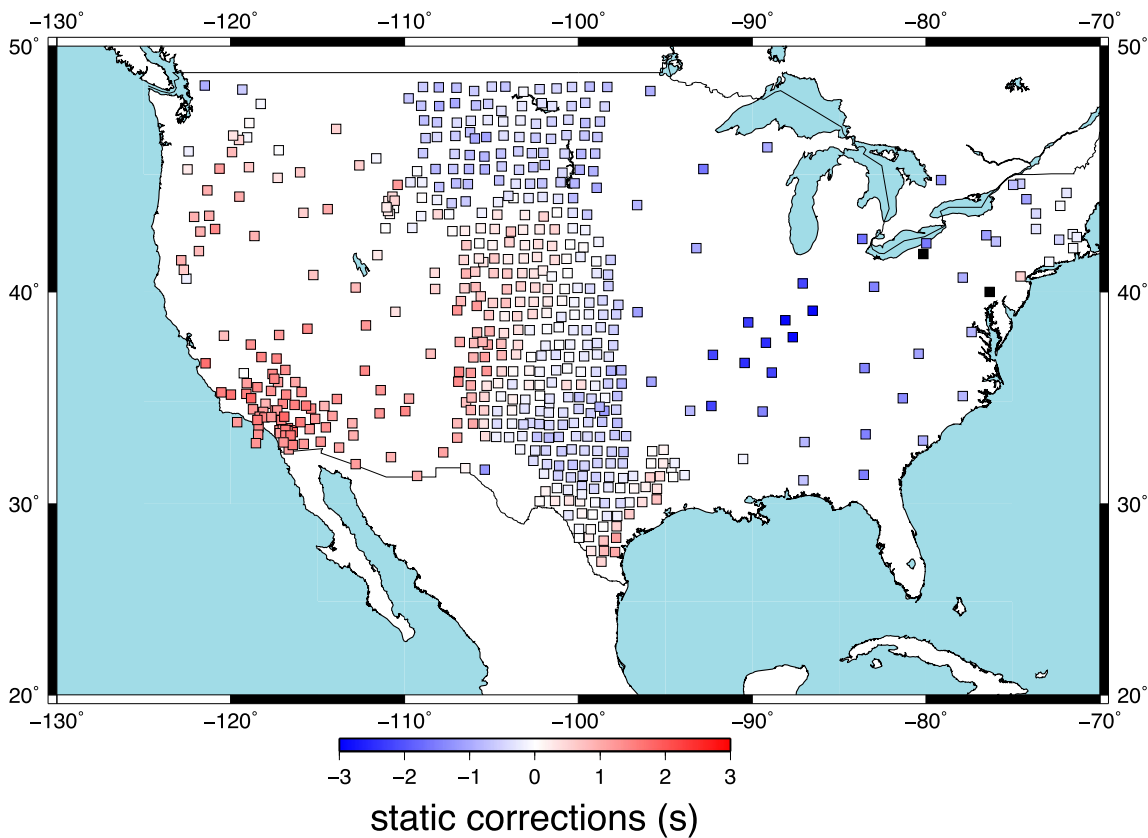**Figure 3.** Map of static station corrections.

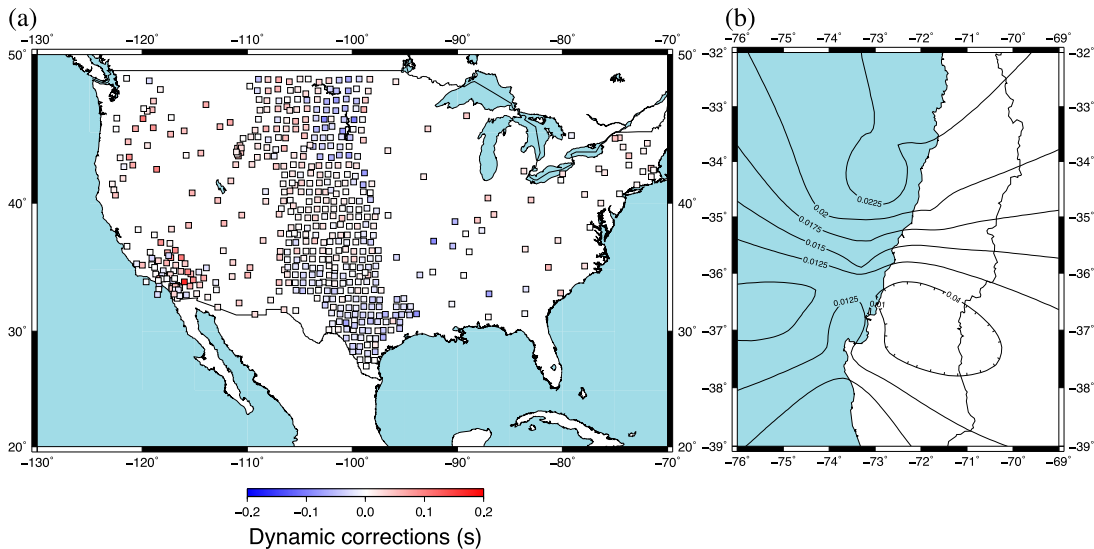**Figure 4.** (a) Example: dynamic corrections for source grid point (34.3°S;73°W). (b) Averaged dynamic corrections for USArray over all the source area. These values have been obtained by averaging the absolute values of the dynamic corrections over all stations.
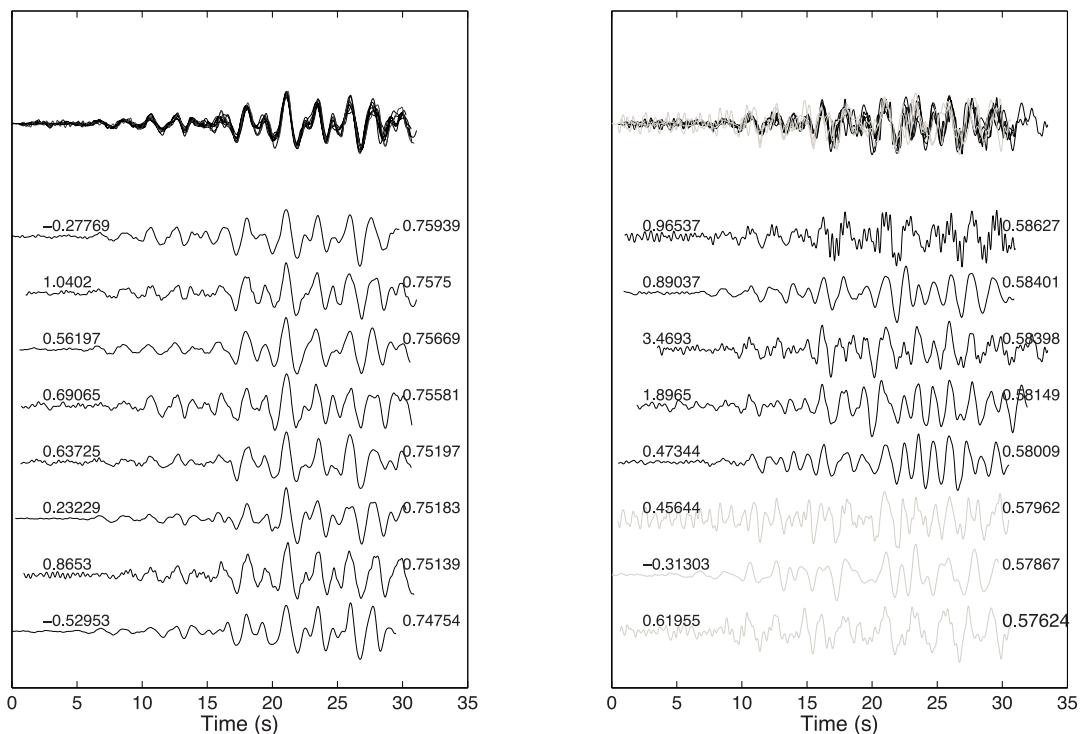

Figure 5. Example of alignment of the traces relative to the M_w 6.3 event of 2011 June 01 filtered between 0.4 and 3 Hz. The traces are sorted by mean cross-correlation coefficients (reported on the right-hand side of the subplots). The traces on the left are those with the highest mean cross-correlation values, and the traces on the right are the traces with cross-correlation coefficients just above and below the threshold. The top trace in each window shows all the traces below overlain in order to visualize the coherence of the traces. In this example, only stations with mean cross-correlation higher than 0.58 were selected (plotted in black). The threshold was empirically selected by visual inspection. The corresponding mean time-shifts (in seconds with respect to the traveltimes predicted by the 1-D velocity model) are indicated on the left within the two subplots.

concentrated in the tectonically active western part of the United States, whereas the eastern United States tends to have early arrivals, as is expected from the well-known contrasts in mantle structure across the United States (Grand 1994). A comparison of the static corrections with the station-based corrections from HC procedure (i.e. calibration based on the main shock catalogue epicentre) shows that the separation in fast and slow regions is common to both the approaches, but the static corrections represent a smaller correc-

tion to the traveltimes predicted by the 1-D velocity model, with a discrepancy mostly lower than ~0.3 s (see Fig. S5).

Fig. 6(a) shows the variogram of dynamic corrections. A nearly linear scaling pattern is visible for distances below about 400 km. In this range, the semivariance is of the order of ~0.01 s², which means typical values of the dynamic corrections equal to ~0.1 s. For larger distances, the semivariance increases up to about 0.02 s², with less stable results above 350 km distance due to the much smaller
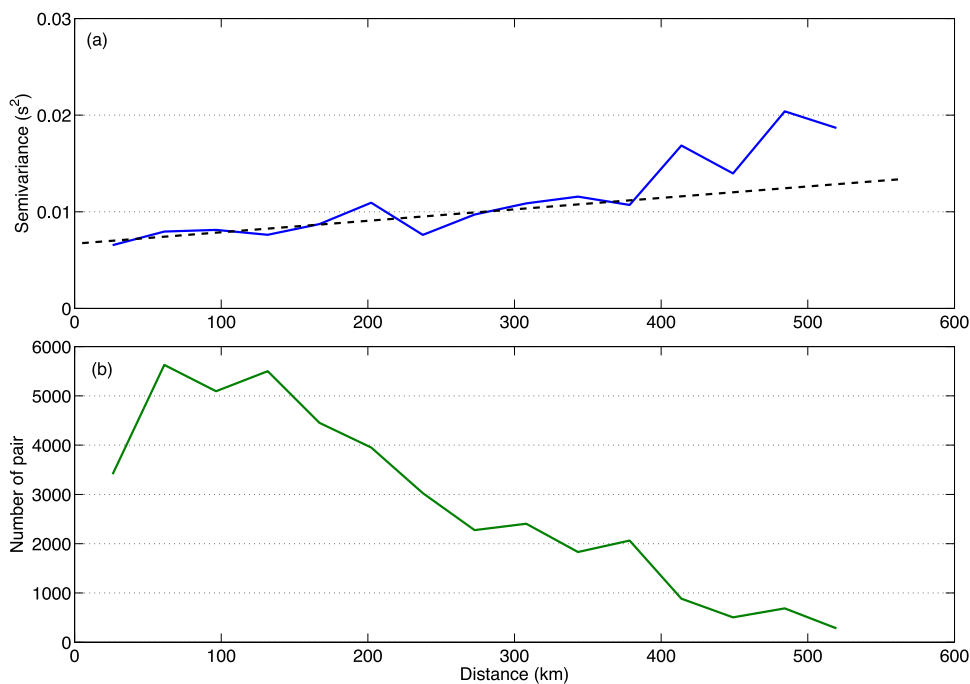
Figure 6. (a) Variogram of the dynamic corrections and (b) number of pairs as function of the distance between the aftershocks. A region of linear scaling is visible for distances shorter than about 400 km. The dotted line in the subplot (a) is the best linear fit (in a least-square sense) of the points for distances below 380 km.

number of pairs per distance bins (Fig. 6b). We model the variogram by a least-square linear fit of range of distances (between aftershock pairs) of 0–380 km; this fit is represented in Fig. 6(a) as a dotted line with slope of $1.25 \times 10^{-5}\, \mathrm{s^2\, km^{-1}}$. Beyond 380 km this variogram model slightly underestimates the observed semi-variance but the effect on the kriging result is minor because both the small number of events at such large distances and their minor absolute weight.

In order to give an impression of the magnitude of dynamic correction terms, we plot the term associated with one gridpoint for all used stations (Fig. 4a) and a contour plot of the source area showing average dynamic terms (Fig. 4b). The typical time corrections are less than 0.2 s, about an order of magnitude less than the static corrections.

3.2 Testing: backprojecting aftershocks

Before moving to the analysis of the main shock, in order to validate the time shifts estimated by kriging, we backproject the aftershocks used for calibration with the complete travel time corrections to check whether we are able to recover the source position used in the calibration procedure. We infer the position of the maximum of the semblance calculated by backprojecting each aftershock filtered in the three frequency bands introduced above. In Fig. 7, we compare the location of these maxima with the catalogue source locations (which were mostly inferred using local networks, see Table 1).

The actual epicentres can be recovered in the vast majority of cases, with the discrepancy mostly below 20 km. A larger distance is associated with the events extracted from the NEIC catalogue (white triangles in Fig. 7), presumably reflecting the larger epicentral error in the global catalogue.

An error in the source location by backprojection can be estimated by the width of the main peak of the semblance over the source area. We examine the variation of semblance with distance from

the maximum by fixing the latitude or longitude corresponding to the position of the maximum. In Figs 8(a)–(d) we show the results for one of the calibration aftershocks (event 16 in Table 1) for the three frequency bands. In the part d, the blue line corresponds to the solution with complete traveltime corrections, whereas the green line is the solution when only static corrections are included. The difference between the maxima of the two curves is mostly contained within one grid spacing and is normally appreciable only at high frequencies, confirming that the dynamic corrections are usually a second-order effect, only causing small changes in the position of the peak semblance.

In all the cases, the curves are well distinguished from the background level and mostly display a symmetric behaviour with a clear peak, which matches the catalogue location (red dotted vertical line). The standard deviation of a Gaussian approximating the peaks of the semblance function is about 40 km for the band 0.4–3 Hz, and about 20 km for 1–4 Hz and 2–8 Hz. For most of the considered events, these values are larger than the discrepancy between the catalogue location and the location of the maximum in the backprojection, suggesting that the actual error is generally much smaller.

Only one time our technique failed in recovering an event: an event close to the southern edge of the source area in the 2–8 Hz band (event 23), for which no coherent arrivals are detected due to a very low signal-to-noise ratio. This event can be recognized in Fig. 7(c) as that for which no circular dots are plotted along with the (white) triangle.

Fig. 8(d) shows that the dynamic corrections only slightly improve on the solutions with only the static corrections. Therefore correcting the traveltimes with only a station-based term will be satisfactory in most cases, as the amplitude of the path-dependent terms normally constitutes only ∼10 per cent of the total time corrections (compare Figs 3 and 4a). Obviously, the actual percentage value will vary with tectonic environment and also distance range. The effects of the dynamic term on the progression of the main
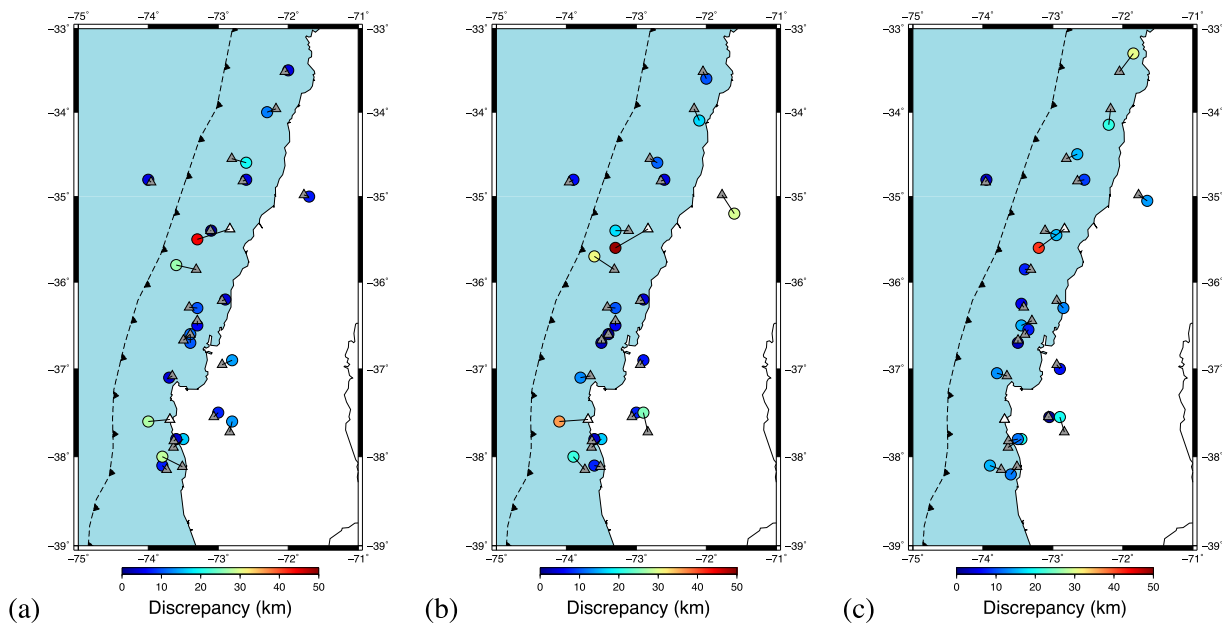
Figure 7. Distance between the epicentres of the calibration aftershocks inferred by backprojection (circles) and by first arrivals recorded by dense seismic local networks (triangles – white triangles mark the NEIC hypocentres). Subplots a, b, c show results for pass bands of 0.4–3, 1–4, 2–8 Hz, respectively.

radiating point during the main shock are displayed in Fig. S6: the shift (if any) of the position of the semblance peak is mostly limited to one gridpoint (i.e. 0.1°). Nevertheless, our calibration procedure shows a better focusing of the spatial distribution of the radiated energy than HC case (see Fig. S7), thus leading to a higher resolution in tracking the radiated energy.

4 RESULTS: IMAGING THE MAIN SHOCK

We now apply the backprojection algorithm to the main shock. The overall time-evolution of the rupture can be examined by considering the maxima of semblance and energy in each time frame (Fig. 9).

On the basis of the amplitude modulation of both semblance and energy, we distinguish five phases of the rupture process, which are highlighted in the figure by vertical dotted lines and labelled with roman numerals I–V. In total, the rupture process appears to last about 160 s. The semblance is highest at the onset of the event, with a loss of coherence later on because of interference from the codas of earlier activated sectors. Especially in this phase, semblance highlights low-energy coherent arrivals, displaying a sharper contrast with the background level than the beam energy (Fig. 9).

For all three frequency bands, energy peaks at around 100 s after the onset. This peak dominates the energy release process in the case of 1–4 Hz, whereas for the 0.4–3 Hz and 2–8 Hz bands, another significant peak appears about 40 s after the onset. The late peak at about 200 s, especially visible in the time-evolution of the semblance at 2–8 Hz, can be interpreted as a very early aftershock occurring shortly after the main shock or as a re-activation of the main slip area in the last phase of the rupture process.

The overall time evolution of the energy shows many similarities with the moment rate function deduced from teleseismic *P* and *SH* waves [Fig. 9, panel e, Delouis *et al.* (2010)]: the overall duration of the rupture is similar and the position of the main peak during phase III approximately matches. However, the energy of the short period

radiation is much more variable with more pronounced differences between active and quiet phases of the rupture. The reduced variability in the finite fault inversion is a natural consequence of the use of much longer periods in the slip model inversion of Delouis *et al.* (2010).

Fig. 10 displays maps of the stacked energy during the five phases for the 1–4 Hz band. This representation also shows the activation of the southern patch of the rupture area, which first appears as a secondary peak in Phase II and migrates southwards during the following phases. The southern limit of the rupture process is highlighted by the radiation emitted in Phase IV and Phase V, which is located south of Arauco peninsula at ∼38°S (see also Fig. S1). The bottom right frame in Fig. 10 shows the emission ∼200 s after the beginning of the rupture, where the patch activated in Phase I is reactivated, but with much lower energy. This can be interpreted as an early aftershock, as there is a short but clearly defined temporal gap to the main rupture.

Globally, the rupture process activates three along-strike segments of the subduction interface, two north of the epicentre and one south of it, with the last one mostly releasing energy below 1 Hz (see Fig. S8).

In order to focus on the details of the rupture, we plot the maximum of the semblance in each time frame (Fig. 11). The onset of the event corresponds to the highest values of semblance, and nearly matches the position of the source based on the first motion polarity detected with high-rate GPS data (Vigny *et al.* 2011). Moving further in time, for all frequency bands, we find an overall north/northeastward migration of the source, in agreement with previous backprojection studies of the Maule event. Moreover, from 70 s after the onset of the rupture process, the general trend is associated with a deepening of the source, which moves towards deeper parts of the subduction interface. The last stage of the rupture process (Phase V, red points in Fig. 11) can only be followed in the frequency bands 0.4–3 Hz and 1–4 Hz, whereas for 2–8 Hz it is hidden by scattering effects.

In Fig. 11, we overlap also the semblance peaks obtained by HC procedure. The difference between some of the peak positions of
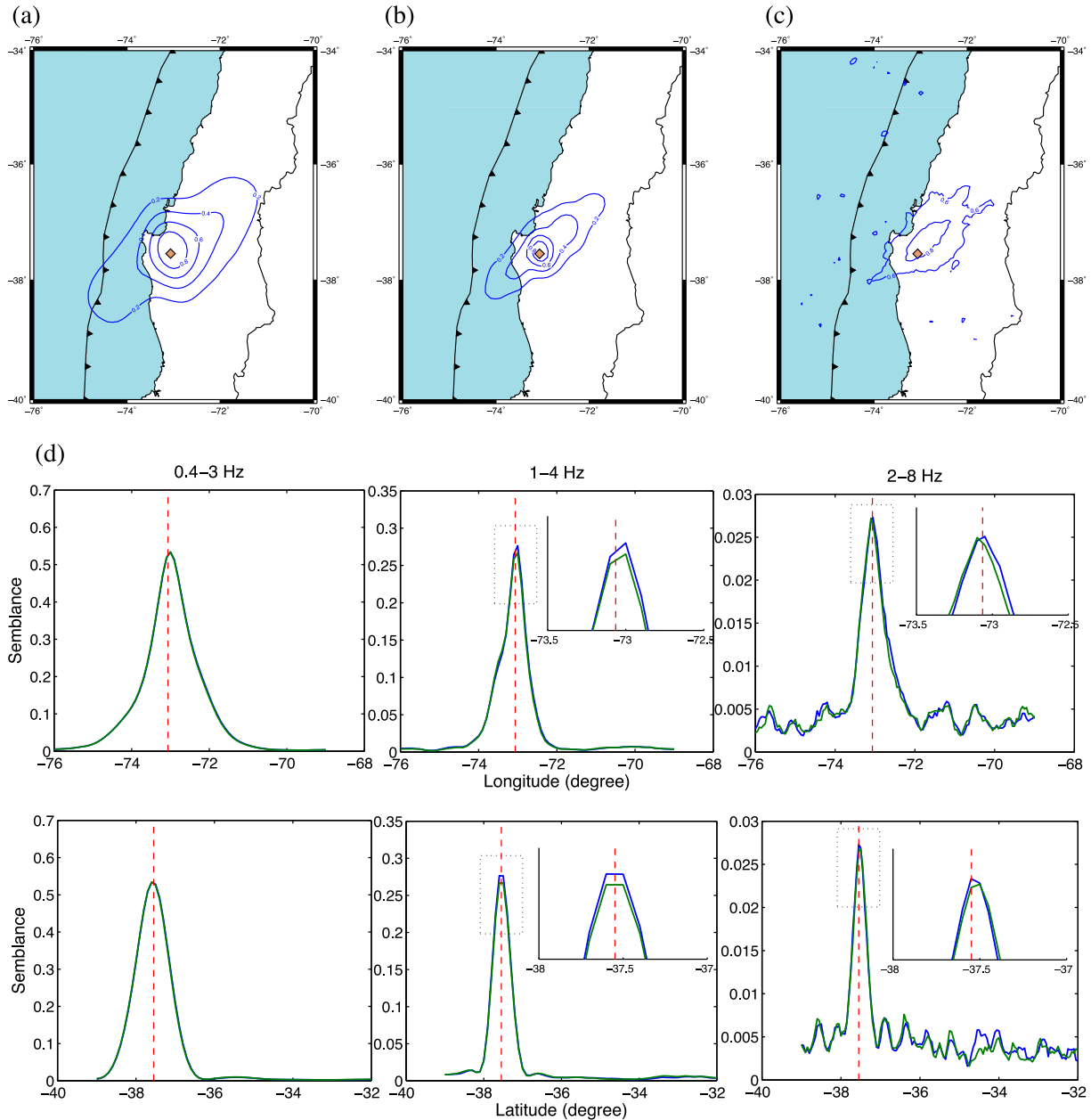
Figure 8. (a–c) Spatial distribution of normalized total energy for event 16 in Table 1 and corresponding catalogue epicentre (yellow diamonds) for frequency bands 0.4–3 Hz (a), 1–4 Hz (b), 2–8 Hz (c); (d) Cross-sections of semblance for the same event, resulting from fixing the latitude and longitude corresponding to the maximum of semblance in the time frame in which it assumes the highest value. Blue and green lines display the semblance distribution including and excluding the dynamic corrections, respectively. The red vertical dotted lines indicate the epicentre as reported in the catalogues. For 1–4 Hz and 2–8 Hz insets of the curves are plotted. In these frequency bands, the improvements induced by dynamic corrections are visible as slight differences in the peak of the function.

the two series is remarkable, especially for low-semblance maxima. Because of the general decrease of the semblance at high frequencies, the threshold semblance values are exceeded in fewer time frames; this reduction is much more pronounced for the results based on the HC procedure, confirming the higher resolution of the procedure described here.

During Phase I and Phase II, a distributed rupture process is reflected by the frequency-dependency of the grid points with the highest semblance. Specifically, in the band 0.4–3 Hz, the semblance maxima jump at first from the epicentre to a deeper part of the interface, then they migrate back to shallow regions, basically following

a line of constant latitude. Then, they scatter within two areas located inland and offshore, with an overall north/northeastward migration. On the other hand, in the other bands, the points share the initial migration towards deeper regions, but then a northwestward migration occurs along inland points and reaching points offshore at about 35°S. During phases III–V, the high-semblance points migrate in a similar way for all passbands considered.

In order to estimate the velocity of propagation of the rupture front, we plot the time evolution of the distance of the semblance maxima from a reference line (Fig. 12). The reference line is approximately perpendicular to the trench and crosses the epicentre
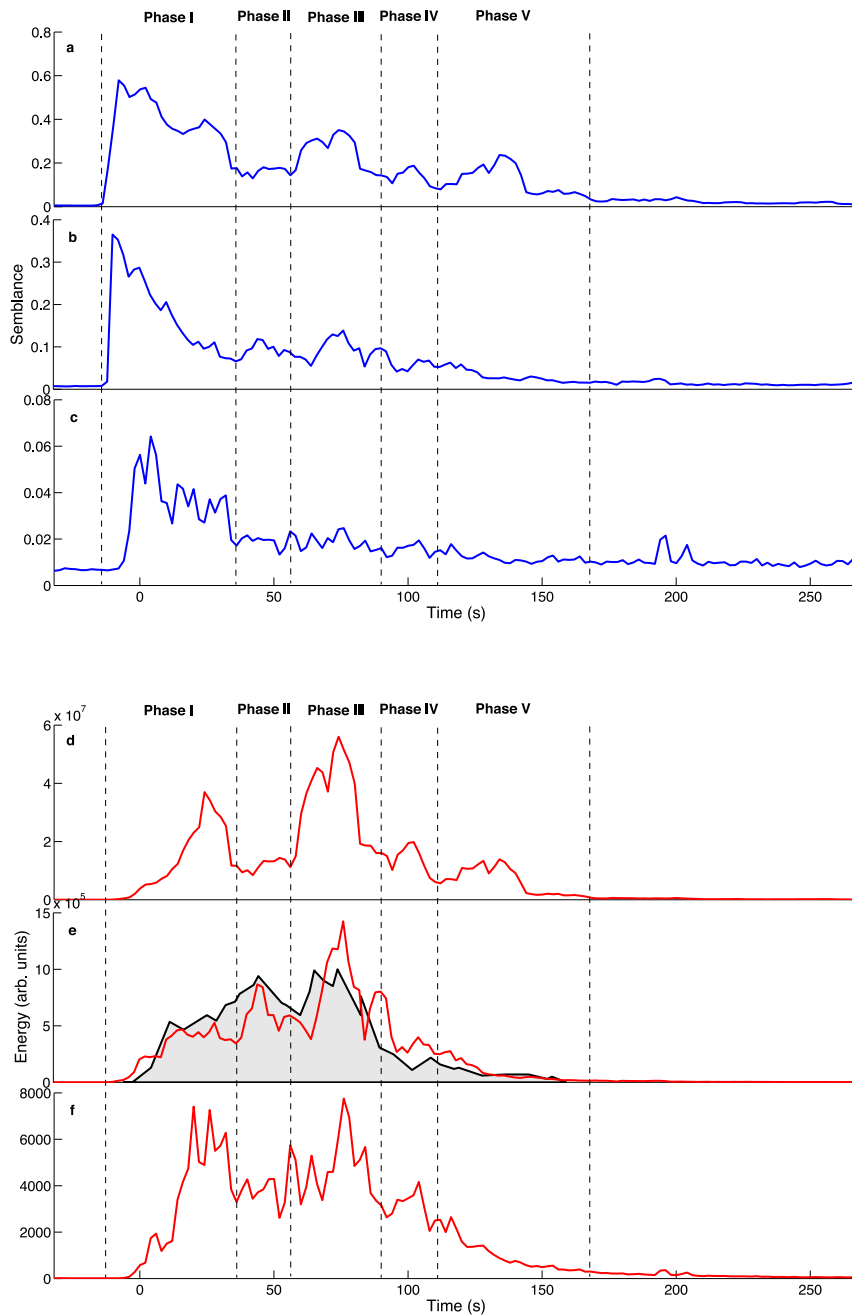
Figure 9. Time-evolution of the maxima of semblance (blue lines) and energy (red lines, arbitrary units) for the three frequency bands: (a,d) 0.4–3 Hz, (b,e) 1–4 Hz, (c,f) 2–8 Hz. Zero of the timescale marks the onset of the rupture—origin time after Vigny *et al.* (2011). The plotted values are the maxima of semblance and energy in each time frame. Time refers to the beginning of the time-window, thus windows beginning at small negative times will already include the onset of the rupture. Continuous black line and grey background in the 1–4 Hz panel shows the moment rate function derived from broad-band global teleseismic *P* and *SH* waves (Delouis *et al.* 2010) for comparison.

(see Transect 2 in Figs 11 and 13). The size of the dots in the figure is proportional to the semblance. We have plotted only the points north of the transect, as too few maxima of semblance are visible in the southern patch of the rupture area to be able to detect a pattern of the rupture front. From this representation, it appears that during the first ∼15–20 s of the rupture process the source is stable, with some variation with frequency. Concurrently with the onset of northward propagation, the rupture jumps eastward, nearly parallel to the reference transect, skipping a distance of 50–60 km along dip,

as visible from inset (d) of Fig. 12. Afterwards, it moves northwards with possibly several minor jumps. For the highest frequency band, we cannot follow the rupture process until the end as scattering effects hide low-energy coherent arrivals.

Looking at the beginning and end of the migration of the maxima of semblance (thus excluding the first ∼20 s of the rupture), we find an overall velocity of the rupture front of about 3 km s^{-1} (violet dotted line in Fig. 12), which is basically equal to the rupture velocity during Phase III–V. During Phase I (including the nucleation phase)
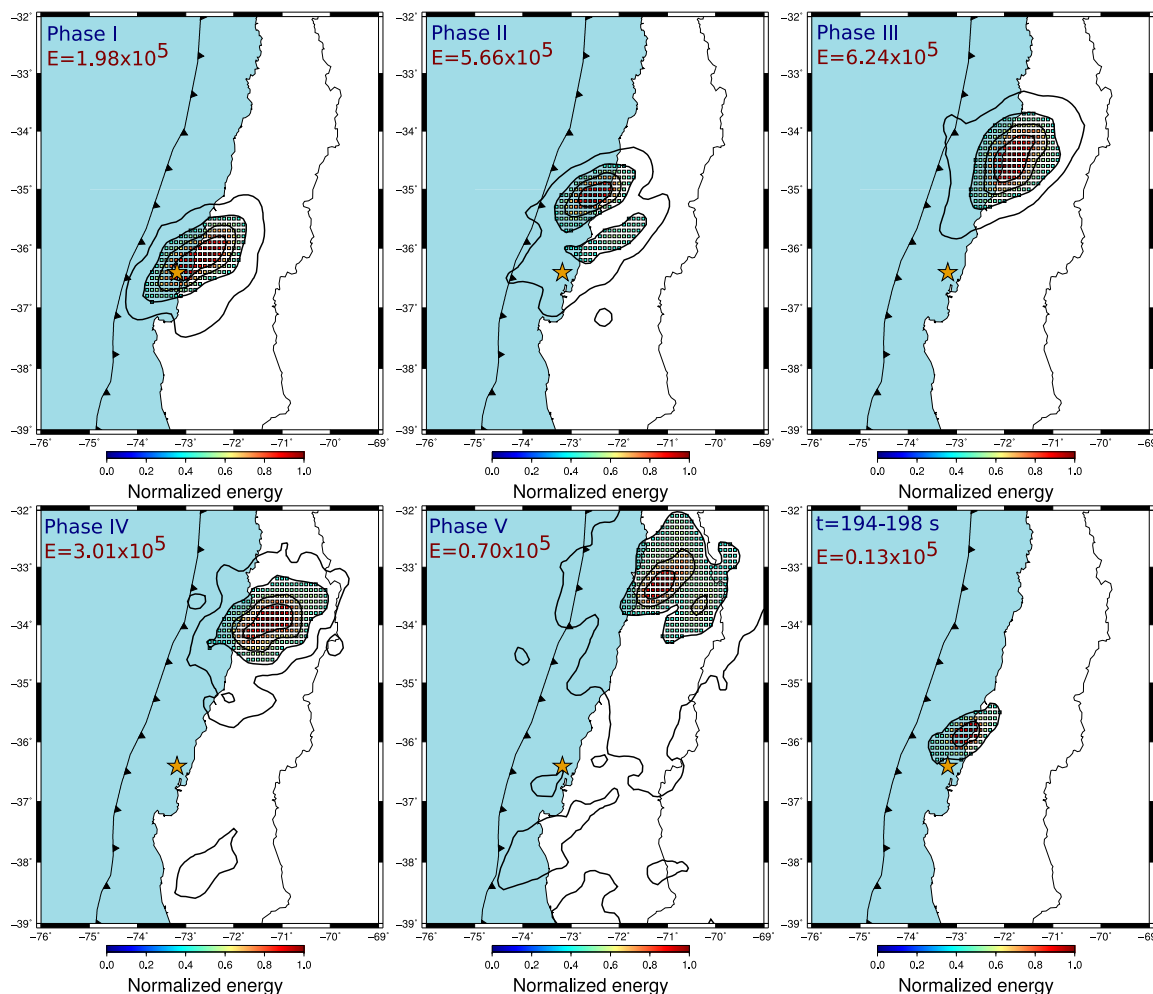
Figure 10. Stacked energy in the 1–4 Hz band during the five phases defined in the text and Fig. 9, and (bottom right) a short time window around the early aftershock at 200 s. The colour scale is normalized to the peak value and gridpoints with values larger than 0.4 of the maximum are highlighted with small squares. For the other bands, see Figs S1 and S2. The normalizing factors (in arbitrary units) are displayed on top left of each subplot and have been estimated as the peak value of the energy averaged over the time frames composing the phase. Note that during the last phase of the main rupture (phase V), the absolute energy has decayed so much that the mapping suffers from a low signal-to-noise ratio.

and II, the complex pattern of rupture propagation (first downdip to the east, then north, then updip again) precludes measurement of a propagation velocity with any accuracy. Kiser & Ishii (2013) split the rupture process into two subevents roughly corresponding to our Phase I and Phase III, for which they find a velocity of 1.9 and 2.7 km s^{-1}, respectively, broadly in line with our findings but implying a slightly slower rupture.

5 BACKPROJECTION RESULTS IN THE CONTEXT OF THE COSEISMIC SLIP AND AFTERSHOCK DISTRIBUTION

In Figs 13–15 we compare the results of the backprojection analysis for the three frequency bands to the distribution of aftershocks and the geodetically inferred coseismic slip.

For all frequency bands, the short period seismic energy release is mostly concentrated downdip of the main coseismic slip, in accordance with prior backprojection results for the Maule (Kiser & Ishii 2011) and Tohoku earthquakes (Meng *et al.* 2011) and other great subduction earthquakes (Lay *et al.* 2012; Yao *et al.* 2013). Moreover, the northern patch of concentrated energy release falls at the

northeastern edge of the coseismic slip, which in turn is colocated with the highest aftershock density. A similar pattern is also visible south of Arauco peninsula, where a secondary peak of energy appears that is just southeast of a relative maximum of the coseismic slip (see the energy contour in Figs 13 and 14 and also phase IV in Fig. 10; as the southern branch of the rupture never becomes dominant and only gives rise to secondary maxima of energy release, no points representing semblance maxima in individual time frames actually plot there). This pattern can be understood from the fact that coherent energy release at short periods is associated with the spatial derivatives of rupture velocities and slip along the rupture surface, rather than with the slip itself.

5.1 Along-dip features

The hypocentres of plate interface aftershocks display a bi-modal distribution, with two preferential distances from the trench and two preferential depths (Lange *et al.* 2012). This behaviour can be seen in the aftershock density plotted in Figs 13–15, where a discontinuous band of seismicity clusters about 30–40 km landward of the coast line is nearly parallel to the trench and detached from and deeper
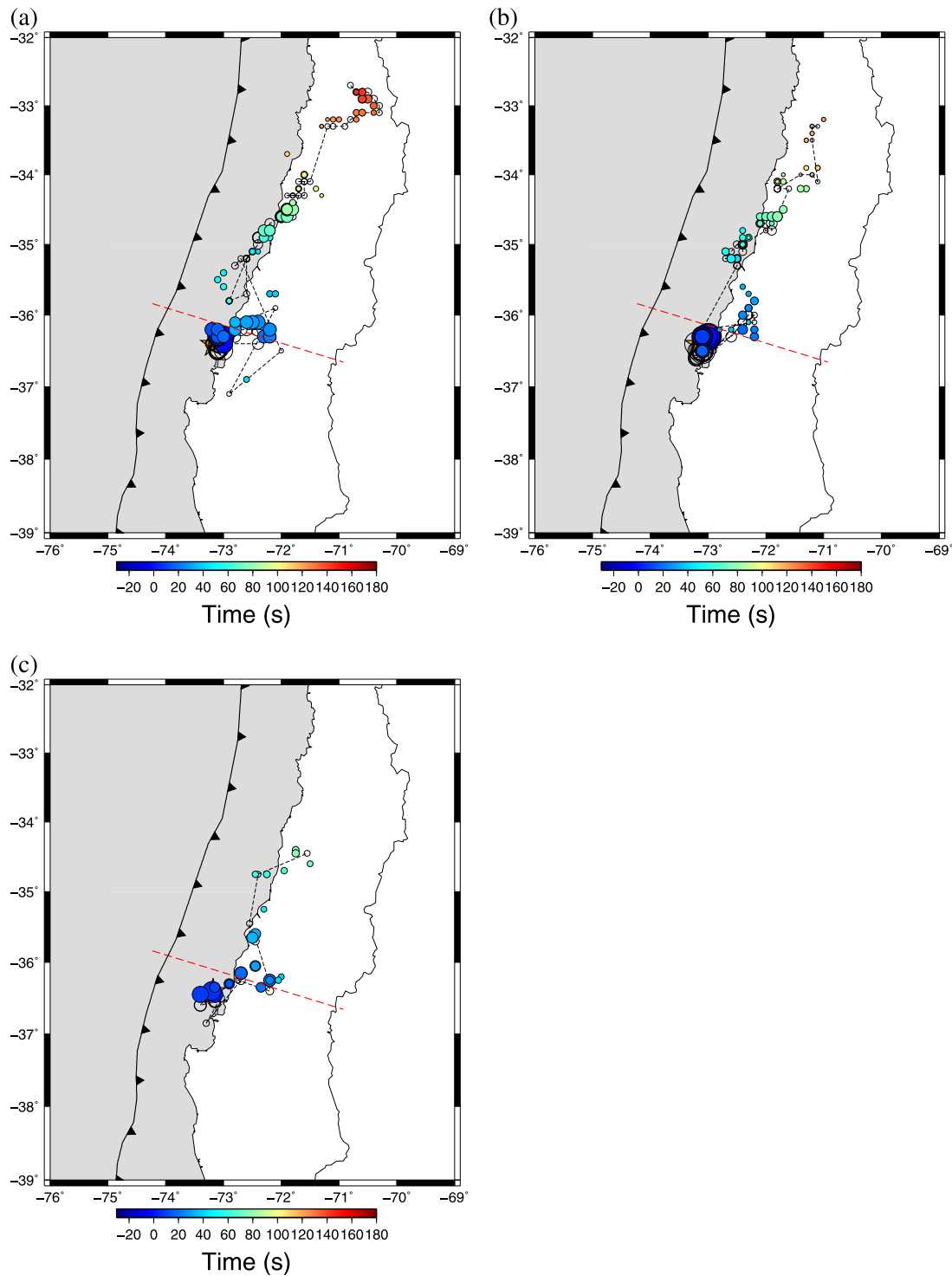
Figure 11. Temporal-spatial evolution of semblance maxima. The size of the circles scales with the value of the semblance, and their colour indicates the time since the catalogue origin time of the main shock. Only points with semblance larger than 0.1, 0.05, and 0.02 have been plotted for the bands 0.4–3 Hz (a), 1–4 Hz (b), and 2–8 Hz (c), respectively. The red line indicates the position of the reference transect cited in the text and corresponding to Transect 2 of Fig. 13. The small black circles connected by a dotted line display the time-evolution of the semblance peaks for travel time corrections calibrated with HC procedure. In plotting these solutions, we use the same semblance thresholds as mentioned above.

than the main group of seismicity just near the coast. As remarked above, during Phase I there is a migration of the source towards deeper parts of the subduction interface followed by a moving back to shallow regions along with a northward propagation, with some of the details varying between frequency bands. What is common to all

bands is that the emission points occupy a similar range of distances to the trench as the aftershocks, that is, the deepest emission points coincide with the depth of the deepest plate interface aftershocks (as we have no control on the depth of energy emission points we assume that the radiation originates from the plate interface).
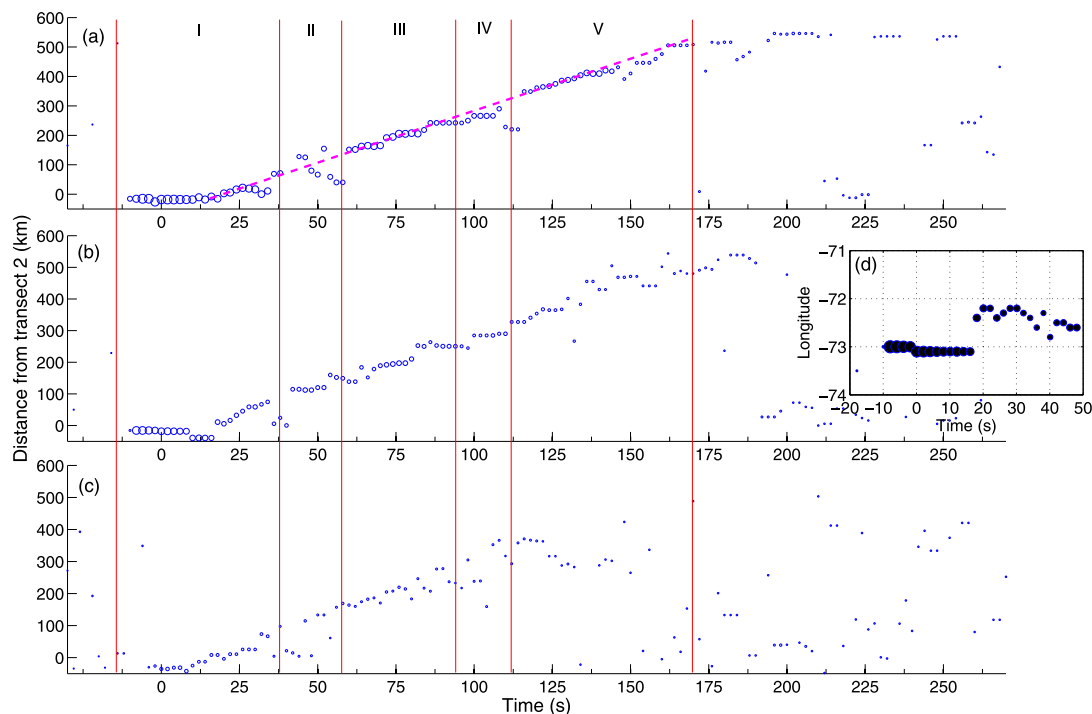
Figure 12. Position of semblance maxima (perpendicular distance to Transect 2, see Fig. 11) versus time since origin time for (a) 0.4–3 Hz, (b) 1–4 Hz and (c) 2–8 Hz. The size of the dots is proportional to the value of semblance. Points falling south of the epicentre are neglected here, as they in few cases represent the global maximum within a time frame. Vertical lines indicate phases of the main event shown in Fig. 9. The violet dotted line in (a) indicates a propagation velocity of 3 km s^{-1} (fitted by eye). (d) Time evolution of the longitude of the maxima of semblance in the band 1–4 Hz showing the 'jump' of the radiation during Phase I. This behaviour is common to all frequency bands.

Whether at any given point in time during the mostly northwards propagating rupture the semblance maxima are at the deeper or shallower end of this range or in between varies somewhat between the different frequency bands. The test with the isolated aftershock (Fig. 8) suggests that the resolution of the method is sufficient to distinguish between emission from the deeper or shallower part. We therefore tentatively conclude that during the northward rupture the areas of both the shallower and deeper plate interface aftershocks are activated simultaneously; which part dominates at any given moment varies as the rupture progresses and also as a function of the considered frequency band.

The question is whether emission affects the whole depth range where plate interface aftershocks occur, or whether the two groups identified in the aftershock seismicity have an equivalence in the short period radiation during the main shock rupture. The 1–4 Hz band probably represents the best compromise between resolution and signal-to-noise ratio, and consequent ability to track rupture emission points. For this band we show histograms of the number of aftershocks in the vicinity of two trench-perpendicular transects (Fig. 16): the northern Transect 1 crosses the areas where most of the energy is emitted (to the northeast of the coseismic slip maximum), and the southern Transect 2 crosses the area just to the northeast of the epicentre, where the highest semblance values are obtained. The above mentioned bimodal distribution is clearly reflected in the double peak of the seismicity histograms, which are separated by ∼45 and ∼60 km for Transect 1 and Transect 2, respectively (Fig. 16). In both transects we see two separate trench distances, at which semblance maxima occur preferentially, with a clearly defined minimum in between at least for Transect 2. Moreover, the peaks of the distribution of semblance maxima correlate with the peaks of the seismicity distribution, and even the relative height of

the peaks appears to be similar. The cumulative radiated energy has a maximum in between the two peaks of the seismicity histogram, in line with the results of Yao *et al.* (2013) for frequencies >0.1 Hz. The energy radiated from distances corresponding to the deeper peak of seismicity is about the 75 per cent of the maximum.

For the other frequency bands the correspondence is not quite as close (see Supporting Information figures): Transect 2 still shows the double peak structure in all bands considered but the alignment at the highest frequency band is not quite as good, although for these frequencies a double peak appears in the cumulative energy profile. Transect 1 is dominated by a single peak, presumably because emission from both parts of the rupture surface interferes and cannot be separated in the other bands. Nevertheless, based on the correspondence within the most clearly defined band, we argue for a close correspondence between areas exhibiting aftershock seismicity months after the main shock and areas activated as emitters of short period seismic waves during the main shock rupture.

In particular, the aseismic gap between both groups visible in the aftershock sequence also appears to have not been activated or only weakly activated during the coseismic rupture. Of course, in the long run, this part of the plate interface must also slip, and we can speculate that it moves by creeping. So far, two models of post-seismic slip covering more than one year have been published (Bedford *et al.* 2013; Lin *et al.* 2013) covering very similar time spans (420 and 488 days after the main shock, respectively) but they differ in how far updip or downdip they place the most intense post-seismic slip. Bedford *et al.* (2013) infer the largest post-seismic slip to occur just downdip of the coseismic slip maximum and mostly to the west of the coast line, whereas Lin *et al.* (2013) infer most of the post-seismic slip to have occurred further downdip to the east of the coast line, and attaining its peak values close to the deeper
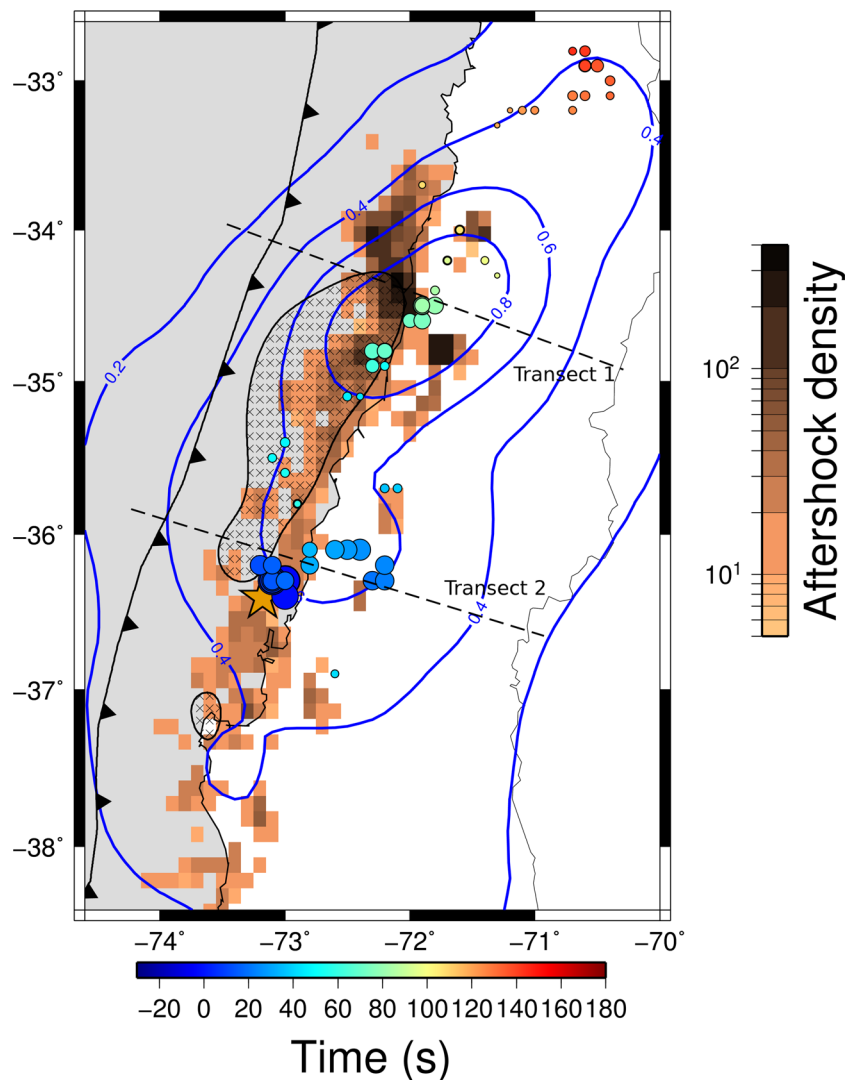
Figure 13. Results of backprojection in the band 0.4–3 Hz together with coseismic slip and aftershocks from previous works. Filled circles display the position of the maxima of semblance (larger than 0.1). Their size is proportional to the semblance and the colour displays the time indicated in the horizontal colourbar. Blue contours show the spatial distribution of the time-integrated released energy. Hatched area displays the coseismic slip larger than 10 m in the Moreno *et al.* (2012) model. The black barbed line represents the trench. The number of the aftershocks per $0.1° \times 0.1°$ cell that have occurred during the first 6 months and were located within 10 km from the slab interface (Lange *et al.* 2012) is represented (in log-scale) by the colours in the background. Only cells hosting more than 10 events are displayed. The big orange star represents the epicentre from Vigny *et al.* (2011). Finally, the black dotted straight lines display the two transects adopted to project the maxima of semblance, the aftershock density and the cumulative energy in Fig. 16. See the text for details.

group of seismicity, albeit only in patches. The differences between both models presumably stem from different assumptions about the geometry of the plate, the rheology of the surrounding material, the chosen regularization and the exact types of data used. Taken together, the afterslip models imply that observed motion within the aseismic gap is compatible with geodetic constraints but that uncertainties in the post-seismic models do not allow to distinguish motion within the gap or the adjacent seismically active areas further up- or downdip.

5.2 Along-strike features

Along strike, we can discern two main emission areas located just to the northeast of the epicentre and in the latitude range 34°–35°S, which display the highest values of time integrated energy in the 2–8 Hz and 1–4 Hz band, respectively (see Figs 14, 15 and S8). These two emission areas are mostly activated during Phase I and

Phase III, respectively. There is no discernable correlation between the latitudinal position of the downdip maxima of the semblance and individual clusters in the deep group of seismicity. The peak at 34°–35°S is shifted noticeably (>50 km) with respect to the coseismic slip maximum but its along-strike extent coincides more or less with the most intense aftershock seismicity. This shift contrasts with the agreement of the time-history of short period-energy release and moment release (Fig. 9). The spatial offset but temporal coincidence can be reconciled if we assume that the deeper part of the rupture, which dominates the emission of short period seismic waves, runs slightly ahead of the shallow part of the rupture, where most of the coseismic slip is accrued. This behaviour actually conforms to the naive expectation of increasing rupture velocity with depth based on the simple fact that shear wave velocities tend to increase with depth, but is unlike the very slow propagation seen along the downdip edge for the first half of the rupture in backprojection studies of the 2011 Tohoku-Oki earthquake (Meng *et al.* 2011).
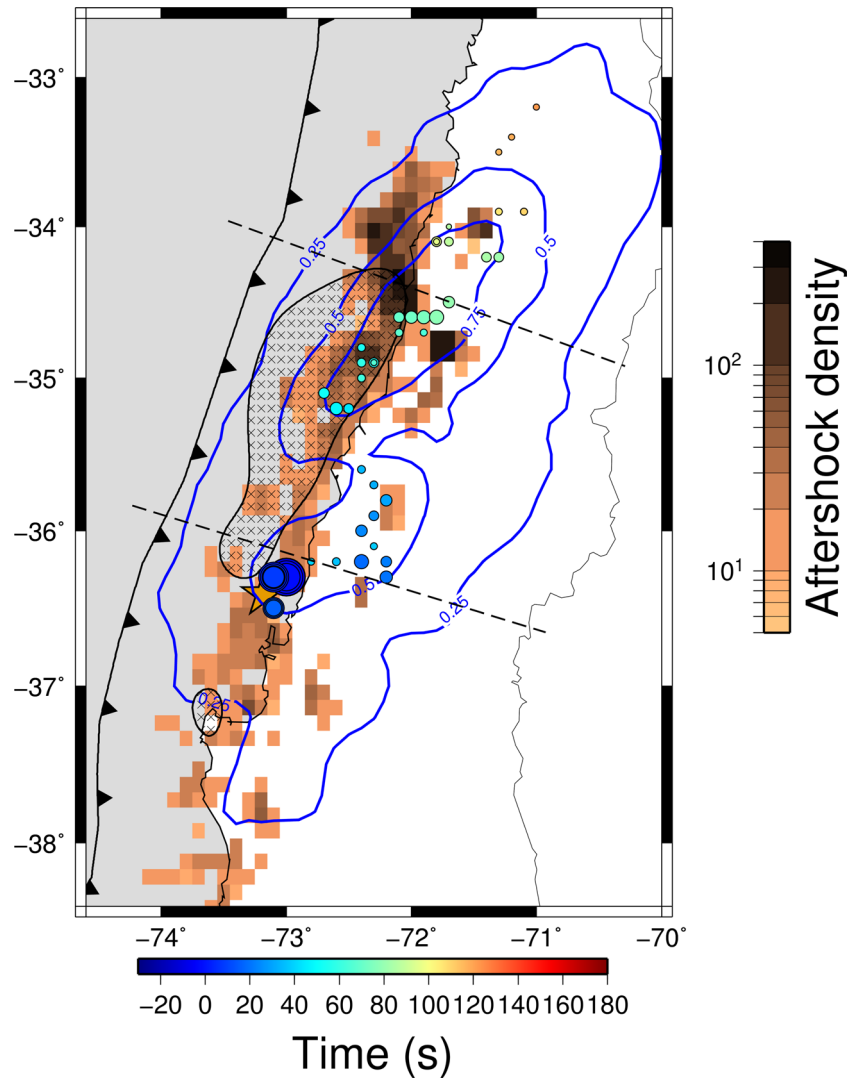
Figure 14. As Fig. 13, but for the band 1–4 Hz. Only solutions with semblance larger than 0.05 are plotted.

The ends of the rupture appear in the latitude ranges 38°–37°S and 34°–33°S in the 1–4 Hz band, showing values of semblance and energy much smaller than the two main peaks introduced above. These areas are located at the edges of the rupture area and are activated during Phase V or at the end of phase IV for the southern limit, i.e. at the end of the northward and southward-propagating rupture processes (see Fig. 10). Thus, this energy emission is mostly associated with the stopping of the rupture front. In the north, the rupture appears to have propagated further north than the rupture area suggested by aftershocks (Lange *et al.* 2012; Rietbrock *et al.* 2012). However, after the end of the rupture, the coda of the previous rupture can create spurious semblance maxima such that the northern limit of the rupture is less well defined than tracking of the most energetic phase of the rupture.

6 DISCUSSION

Overall, the most striking observation is the fairly close correspondence between the emission of short period seismic waves during the main shock rupture and the aftershock activity. A plate interface with heterogeneous frictional properties could cause the variability

in slip or rupture velocity during the main shock, which is needed to explain the continuous radiation of short period seismic waves and would at the same time provide the heterogeneity in local stress able to explain the aftershock activity. Notwithstanding this overall agreement in the patterns of short period emission and aftershocks, when viewed along-strike and for the deepest part of the seismogenic plate interface, the main rupture appears to radiate from gaps in the deeper belt of plate interface aftershocks, and some major interface events like the M_w = 7.1 earthquake in 2012 (Kiser & Ishii 2013) appear to fill in gaps in the short period radiation.

As similar areas appear to get activated by aseismic afterslip (Bedford *et al.* 2013), significant parts of the plate interface must be capable to move by ductile processes or show velocity-strengthening frictional behaviour. The interpretation for this pattern is sometimes given as that of a region near the brittle–ductile transition with brittle (velocity-weakening) asperities embedded within a ductile (or velocity-strengthening) matrix (e.g. Perfettini & Avouac 2004; Meng *et al.* 2011). However, if this picture is to be applied to the Maule rupture zone, then the gaps between brittle asperities must be small enough that the rupture can proceed essentially unimpeded at normal rupture velocity. Lange *et al.* (2014) found that during the post-seismic phase of the Maule and other recent great
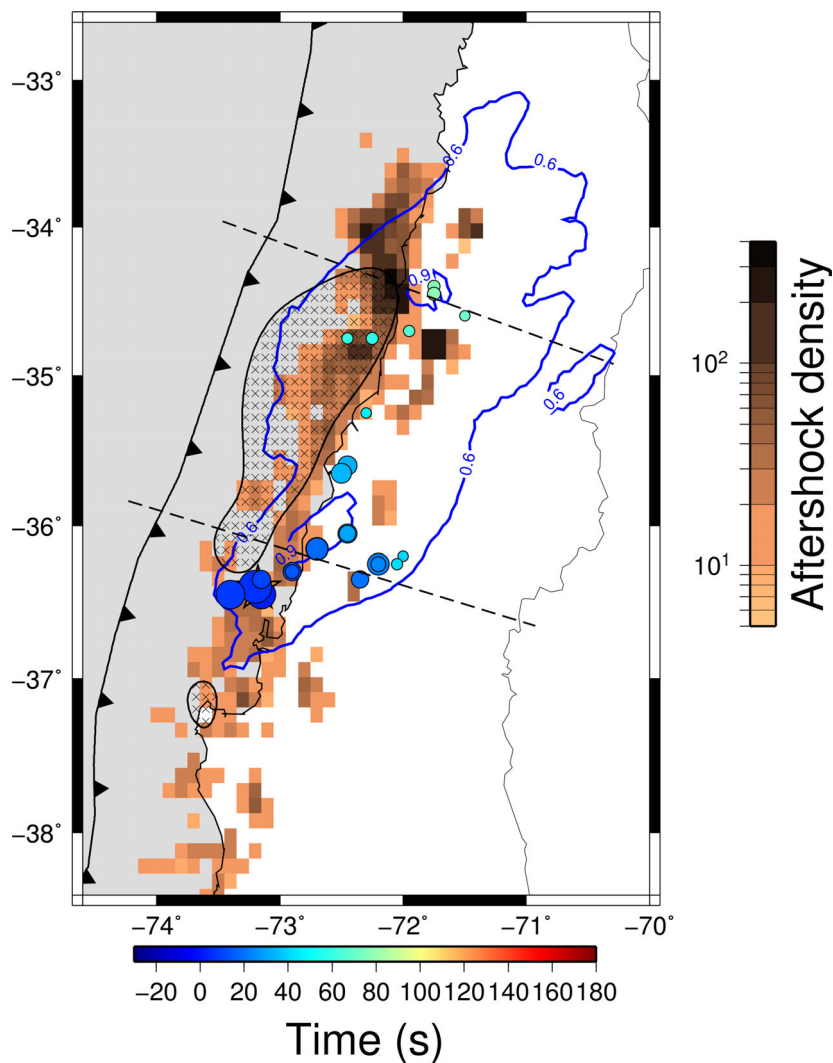
Figure 15. As Fig. 13, but for the band 2–8 Hz. Only solutions with semblance larger than 0.02 are plotted.

subduction earthquakes, although the total post-seismic moment budget is dominated by aseismic afterslip, the cumulative slip of the largest aftershocks locally dominates over aseismic slip, which also emphasizes the role of brittle processes. A further possibility is that the large velocity perturbation during the main rupture actually changes the frictional behaviour to favour brittle failure, following the prediction for conditionally stable parts of the frictional regime (Scholz 2002). Unlike for the shallow parts of the plate interface the conditionally frictional regime does not appear to cause slow rupture, though.

The seismogenic zone has recently been subdivided in a shallower part dominated by co-seismic slip and a deeper part characterized by high-frequency radiation, and the occurrence of major but not great earthquakes in the interseismic period (Lay *et al.* 2012; Schurr *et al.* 2013; Yao *et al.* 2013). Our results—with the co-location of aftershocks and the peak of energy emission at the downdip edge of the coseismic slip area – are in line with this general behaviour. A feature unique to the Maule earthquake is the separation of the plate interface aftershocks into two groups which are spatially separated by a clear gap, which can also be identified in the position of semblance maxima of the backprojection results. It appears likely that deformation within the gap is aseismic both during the coseismic rupture and during the post-seismic phase, suggesting that a first

transition from brittle to ductile behaviour at the downdip edge of the shallower group of plate interface seismicity (and semblance maxima) is followed by a transition back to brittle behaviour. Evidence for a second brittle belt exists along nearly the complete rupture length in the form of either aftershocks or high-frequency seismic radiation, although not necessarily always both in the same spot (Figs 13–15 and 16). This is then followed by the final downdip transition to ductile behaviour at a distance of 150–160 km to the trench. We defer a more detailed exploration of the doubled transition zone to a future publication.

7 CONCLUSIONS

We have backprojected the Maule earthquake (M_w 8.8, Chile, 2010 February 27) calibrating the traveltimes with 23 well-located aftershocks covering the entire slip area, thus associating a specific time correction to each potential emission point in the source area. We have processed three frequency bands: 0.4–3 Hz, 1–4 Hz and 2–8 Hz. The calibration procedure results in a small improvement (at least for the analysed tectonic environment) in the coherence of the main peak with respect to the case when only static station-based traveltime corrections are adopted, but in an increase of the resolu-
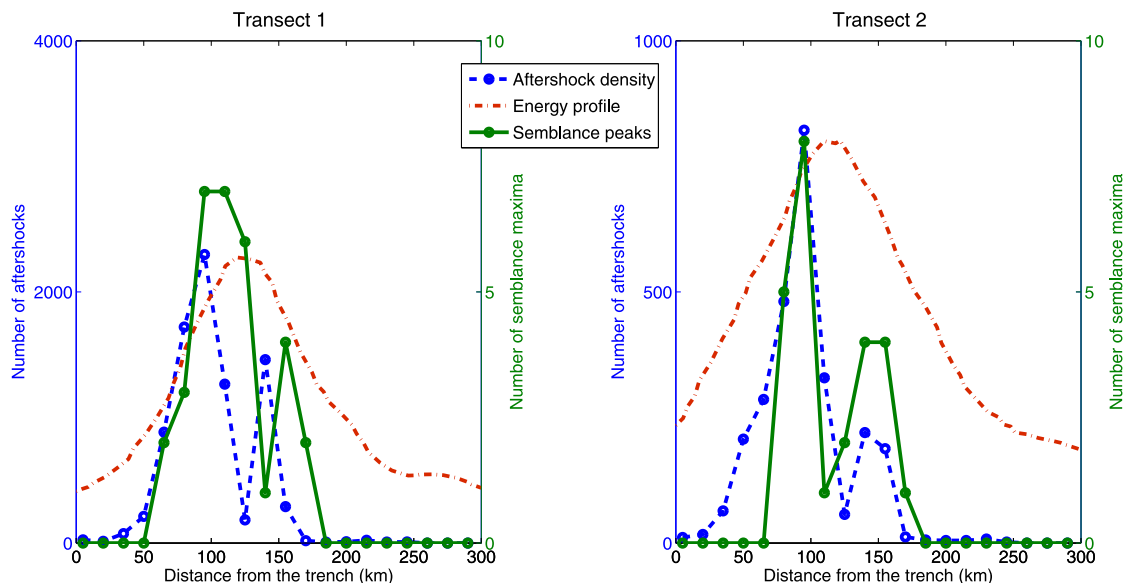
Figure 16. Histogram of number of aftershocks (blue line) and semblance maxima (green line) falling within 100 km either side of the trench-perpendicular transects (location of transects shown in Fig. 13) for 1–4 Hz results. A bin width of 15 km in distance has been used and the points are plotted at the centre of each bin. The aftershocks are taken from the Lange *et al.* (2012) catalogue, restricted to events within 10 km of the SLAB1.0 (Hayes & Wald 2009) plate interface, the same set as used for the earthquake density in Figs 13–15. Only semblance maxima larger than 0.05 are plotted. The profiles of the (normalized) cumulative energy along the two transects are displayed as point-dotted red lines. Figures for the other frequency bands are shown in Figs S3 and S4.

tion with respect to the case in which the traveltimes are calibrated at the hypocentre. The main advantage of the proposed procedure is that the final backprojection result is independent of errors in the hypocentre and is instead tied to the well located aftershocks used for calibration, such that it is possible to interpret the position of semblance maxima with respect to the aftershock patterns and other features determined based on data local to the rupture area, for example geodetically inferred coseismic slip.

We distinguish five phases of the rupture process from the semblance/energy time function. The entire rupture process lasts about three minutes, with most of the energy released during Phase III in an area about 150 km northeast of the epicentre, which is offset to the northeast and downdip from the peak slip, but matches the area of most intense aftershock activity.

Phase I lasts about 40 s and includes an initial low-energy stage of the rupture [taking place near the source position recovered by high-rate GPS data (Vigny *et al.* 2011)] followed by a migration of the source of the seismic radiation towards deeper points, overlapping the position of the deeper cluster of the aftershock seismicity. Then, the rupture front propagates bilaterally, with a general deepening of the front during its northward migration. The southern and northern ends of the rupture fall respectively south of Arauco peninsula and around the position (33°S,71°W), implying an overlap with both the 1960 megathrust earthquake and its foreshocks at the southern end and with the 1985 megathrust event in the north.

The range of distances to the trench from which energy is emitted mostly matches the range of the aftershocks. For the 1–4 Hz band it can be argued that seismic energy is preferentially emitted from two along-dip disconnected belts of the subduction interface, which is apparent especially during the beginning of the event (Phase I and Phase II), when the emitted energy is still relatively low and the two belts are separately activated. Afterwards, during the highest-energy phase of the rupture (phase III), the gap in emission points separating the two belts is not as clearly defined but still present.

A widely accepted scheme distinguishes a seismogenic belt of the subduction interfaces dominated by velocity-weakening regime

bounded up- and downdip by aseismic regions with velocity-strengthening behaviour (Scholz 2002). Recently, the seismogenic zone has been further subdivided in a shallower part dominated by coseismic slip and a deeper part displaying large high-frequency radiation and aftershocks' density (Lay *et al.* 2012). In agreement with this scheme, we find that the peak of energy emission falls at the downdip edge of the coseismic slip area and matches the source area of most aftershocks. However, the existence of a double belt of seismicity and of seismic radiation leads to the hypothesis of an even more complex frictional regime.

REFERENCES

Ammon, C.J. *et al.*, 2005. Rupture process of the 2004 Sumatra-Andaman Earthquake, *Science,* **308,** 1133–1139.

Barrientos, S.E., 1988. Slip distribution of the 1985 central Chile earthquake, *Tectonophysics,* **145**(3), 225–241.

Bedford, J. *et al.*, 2013. A high-resolution, time-variable afterslip model for the 2010 Maule Mw = 8.8, Chile megathrust earthquake, *Earth planet. Sci. Lett.,* **383**(0), 26–36.

Cifuentes, I.L., 1989. The 1960 Chilean Earthquakes, *J. geophys. Res.,* **94**(B1), 665–680.

Cressie, N., 1993. *Statistics for Spatial Data,* rev. edn, John Wiley & Sons Inc..

Darwin, C., Sowerby, G.B., Lonsdale, W. & Forbes, E., 1895. *Geological Observations on the Volcanic Islands and Parts of South America Visited During the Voyage of HMS" Beagle",* D. Appleton and company.

Delouis, B., Nocquet, J.-M. & Vallée, M., 2010. Slip distribution of the February 27, 2010 Mw = 8.8 Maule earthquake, central Chile, from static and high-rate GPS, InSAR, and broadband teleseismic data, *Geophys. Res. Lett.,* **37**(17), doi:10.1029/2010GL043899.

Grand, S., 1994. Mantle shear structure beneath the Americas and surrounding oceans, *J. geophys. Res.,* **99**(B6), 11 591–11 621.

Hayes, G.P. & Wald, D.J., 2009. Developing framework to constrain the geometry of the seismic rupture plane on subduction interfaces a priori—a probabilistic approach, *J. geophys. Res.,* **176**(3), 951–964.

Hayes, G.P., Bergman, E., Johnson, K.L., Benz, H.M., Brown, L. & Meltzer, A.S., 2013. Seismotectonic framework of the 2010 February 27 Mw 8.8 Maule, Chile earthquake sequence, *Geophys. J. Int.,* **195**(2), 1034–1051.

Hicks, S.P., Rietbrock, A., Haberland, C.A., Ryder, I., Simons, M. & Tassara, A., 2012. The 2010 Mw 8.8 Maule, Chile earthquake: nucleation and rupture propagation controlled by a subducted topographic high, *Geophys. Res. Lett.,* **39**(19), doi:10.1029/2012GL053184.

Ishii, M., Shearer, P.M., Houston, H. & Vidale, J.E., 2005. Extent, duration and speed of the 2004 Sumatra–Andaman earthquake imaged by the Hi-Net array, *Nature,* **435**(7044), 933–936.

Ishii, M., Shearer, P.M., Houston, H. & Vidale, J.E., 2007. Teleseismic P wave imaging of the 26 December 2004 Sumatra-Andaman and 28 March 2005 Sumatra earthquake ruptures using the Hi-net array, *J. geophys. Res.: Solid Earth (1978–2012),* **112**(B11), doi:10.1029/2006jb004700.

Kennett, B., Engdahl, E. & Buland, R., 1995. Constraints on seismic velocities in the Earth from traveltimes, *Geophys. J. Int.,* **122**(1), 108–124.

Kiser, E. & Ishii, M., 2011. The 2010 Mw 8.8 Chile earthquake: Triggering on multiple segments and frequency-dependent rupture behavior, *Geophys. Res. Lett.,* **38**(7), doi:10.1029/2011GL047140.

Kiser, E. & Ishii, M., 2013. The 2010 Maule, Chile, coseismic gap and its relationship to the 25 March 2012 Mw 7.1 earthquake, *Bull. seism. Soc. Am.,* **103**(2A), 1148–1153.

Koper, K.D., Hutko, A.R., Lay, T. & Sufri, O., 2012. Imaging short-period seismic radiation from the 27 February 2010 Chile (Mw 8.8) earthquake by back-projection of P, PP, and PKIKP waves, *J. geophys. Res.,* **117,** B02308, doi:10.1029/2011JB008576.

Krüger, F. & Ohrnberger, M., 2005. Tracking the rupture of the Mw = 9.3 Sumatra earthquake over 1,150 km at teleseismic distance, *Nature,* **435**(7044), 937–939.

Lange, D. *et al.*, 2012. Aftershock seismicity of the 27 February 2010 *M*w 8.8 Maule earthquake rupture zone, *Earth planet. Sci. Lett.,* **317,** 413–425.

Lange, D. *et al.*, 2014. Comparison of postseismic afterslip models with aftershock seismicity for three subduction-zone earthquakes: Nias 2005, Maule 2010 and Tohoku 2011, *Geophys. J. Int.,* doi:10.1093/gji/ggu292.

Lay, T., Kanamori, H., Ammon, C.J., Koper, K.D., Hutko, A.R., Ye, L., Yue, H. & Rushing, T.M., 2012. Depth-varying rupture properties of subduction zone megathrust faults, *J. geophys. Res.: Solid Earth (1978–2012),* **117**(B4), doi:10.1029/2011JB009133.

Lin, Y.-n.N. *et al.*, 2013. Coseismic and postseismic slip associated with the 2010 Maule Earthquake, Chile: characterizing the Arauco Peninsula barrier effect, *J. geophys. Res.: Solid Earth,* **118,** 3142–3159.

Lorito, S. *et al.*, 2011. Limited overlap between the seismic gap and coseismic slip of the great 2010 Chile earthquake, *Nat. Geosci.,* **4**(3), 173–177.

Melnick, D., Bookhagen, B., Strecker, M.R. & Echtler, H.P., 2009. Segmentation of megathrust rupture zones from fore-arc deformation patterns over hundreds to millions of years, Arauco peninsula, Chile, *J. geophys. Res.,* **114,** doi:10.1029/2008JB005788.

Meng, L., Inbal, A. & Ampuero, J.-P., 2011. A window into the complexity of the dynamic rupture of the 2011 Mw 9 Tohoku-Oki earthquake, *Geophys. Res. Lett.,* **38**(7), doi:10.1029/2011GL048118.

Moreno, M. *et al.*, 2012. Toward understanding tectonic control on the *M*w 8.8 2010 Maule Chile earthquake, *Earth planet. Sci. Lett.,* **321,** 152–165.

Moreno, M.S., Bolte, J., J., K. & Melnick, D., 2009. Impact of megathrust geometry on inversion of coseismic slip from geodetic data: application to the 1960 Chile earthquake, *Geophys. Res. Lett.,* **36,** L16310, doi:10.1029/2009GL039276.

Neidell, N. & Taner, M.T., 1971. Semblance and other coherency measures for multichannel data, *Geophysics,* **36**(3), 482–497.

Perfettini, H. & Avouac, J.-P., 2004. Postseismic relaxation driven by brittle creep: a possible mechanism to reconcile geodetic measurements and the decay rate of aftershocks, application to the Chi-Chi earthquake, Taiwan, *J. geophys. Res.: Solid Earth (1978–2012),* **109**(B2), doi:10.1029/2003JB002488.

Pesicek, J., Engdahl, E., Thurber, C., DeShon, H. & Lange, D., 2012. Mantle subducting slab structure in the region of the 2010 M8.8 Maule earthquake (30–40 S), Chile, *Geophys. J. Int.,* **191**(1), 317–324.

Pollitz, F.F. *et al.*, 2011. Coseismic slip distribution of the February 27, 2010 Mw 8.8 Maule, Chile earthquake, *Geophys. Res. Lett.,* **38,** L09309, doi:10.1029/2011GL047065.

Rietbrock, A., Ryder, I., Hayes, G., Haberland, C., Comte, D., Roecker, S. & Lyon-Caen, H., 2012. Aftershock seismicity of the 2010 Maule Mw = 8.8, Chile, earthquake: correlation between co-seismic slip models and aftershock distribution?, *Geophys. Res. Lett.,* **39**(8), L08310, doi:10.1029/2012GL051308.

Rössler, D., Krüeger, F., Ohrnberger, M. & Ehlert, L., 2010. Rapid characterisation of large earthquakes by multiple seismic broadband arrays, *Nat. Hazards Earth Syst. Sci.,* **10**(4), 923–932.

Rost, S. & Thomas, C., 2002. Array seismology: methods and applications, *Rev. Geophys.,* **40**(3), 1008, doi:10.1029/2000RG000100.

Ruiz, S. *et al.*, 2013. The Constitución earthquake of 25 March 2012: a large aftershock of the Maule earthquake near the bottom of the seismogenic zone, *Earth planet. Sci. Lett.,* **377,** 347–357.

Scholz, C.H., 2002. *The Mechanics of Earthquakes and Faulting,* Cambridge Univ. Press.

Schurr, B., Asch, G., Rosenau, M., Wang, R., Oncken, O., Barrientos, S., Salazar, P. & Vilotte, J.P., 2013. The 2007 M7.7 Tocopilla northern Chile earthquake sequence—implications for along-strike and down-dip rupture segmentation and megathrust frictional behavior, *J. geophys. Res.,* **117,** B05305, doi:10.1029/2011JB009030.

Trauth, M.H., Gebbers, R., Marwan, N. & Sillmann, E., 2010. *MATLAB Recipes for Earth Sciences,* Springer.

Vigny, C. *et al.*, 2011. The 2010 Mw 8.8 Maule megathrust earthquake of central Chile, monitored by GPS, *Science,* **332**(6036), 1417–1421.

Wang, D. & Mori, J., 2011. Frequency-dependent energy radiation and fault coupling for the 2010 Mw8.8 Maule, Chile, and 2011 Mw9. 0 Tohoku, Japan, earthquakes, *Geophys. Res. Lett.,* **38**(22), L22308, doi:10.1029/2011GL049652.

Yagi, Y., Nakao, A. & Kasahara, A., 2012. Smooth and rapid slip near the Japan trench during the 2011 Tohoku-Oki earthquake revealed by a hybrid back-projection method, *Earth planet. Sci. Lett.,* **355,** 94–101.

Yao, H., Shearer, P.M. & Gerstoft, P., 2013. Compressive sensing of frequency-dependent seismic radiation from subduction zone megathrust ruptures, *Proc. Natl. Acad. Sci.,* **110**(12), 4512–4517.

APPENDIX: A SHORT DESCRIPTION OF KRIGING

Kriging is a spatial interpolation technique, which is based on the assumption of distance-dependent variance. This assumption is expressed as an estimated semi-variogram, which measures the variability of an observable in space. Specifically, a variogram is the distribution of the semivariance of spatially separated observations as function of the distance. This is estimated from the mean squared differences between data points with coordinates $\mathbf{x}_i$ and associated with values $z(\mathbf{x}_i)$ within pre-defined bins of distance (Cressie 1993; Trauth *et al.* 2010).

$$\gamma(h) = \frac{1}{L(h)} \sum_{i,j} \frac{1}{2} \left[z(\mathbf{x}_i) - z(\mathbf{x}_j) \right]^2, \qquad (A1)$$

where the summation is over all *i, j* for which $h \leq |\mathbf{x}_i - \mathbf{x}_j| < h + \delta h$; δh is the binning width for the distance axis, and $L(h)$ is the number of pairs with distances between h and $h + \delta h$. If the stochastic component of a spatio-temporal process is autocorrelated

on a certain length scale, a scaling region appears in which the variance of the observations increases with distance until it reaches a plateau. This implies that closer observations are, on average, more correlated than widely separated ones over a certain range of distances, above which there is no distance-dependency. Conversely, even very close data points generally do not have the same z values due to measurement errrors or very short range phenomena (called the nugget effect in the kriging literature).

We model the variogram in the scaling region by a linear model, from which we interpolate the path effects on the grid points. In detail, for each point $\mathbf{x}_0$, the predicted value ($\hat{z}(\mathbf{x}_0)$) is a weighted sum of all observed data ($z(\mathbf{x}_i)$), with suitable weights (λ_i) being determined by kriging (Trauth *et al.* 2010):

$$\hat{z}(\mathbf{x}_0) = \sum_{i=1}^{M} \lambda_i z(\mathbf{x}_i), \tag{A2}$$

where M is the number of observations. Kriging minimizes the standard error of the estimated $\hat{z}(\mathbf{x}_0)$, which for a given set of λ_i can be calculated from the semi-variograms, under the constraint that the sum of the weights is equal to 1 (to guarantee unbiased estimates). This optimization problem is solved using a Lagrangian multiplier ν, which together with the weights forms vector F (Trauth *et al.* 2010):

$$F = [\lambda_1, \lambda_2, \dots, \lambda_M, \nu]. \tag{A3}$$

The weights are found by solving a linear system of $M+1$ equations in $M+1$ unknowns:

$$F = G_{\text{mod}}^{-1} \cdot G_R; \tag{A4}$$

where G_{mod} is the matrix of coefficients:

$$\begin{bmatrix} 0 & \gamma(\mathbf{x}_1, \mathbf{x}_2) & \cdots & \gamma(\mathbf{x}_1, \mathbf{x}_M) & 1 \\ \gamma(\mathbf{x}_2, \mathbf{x}_1) & 0 & \cdots & \gamma(\mathbf{x}_2, \mathbf{x}_M) & 1 \\ \vdots & \vdots & \vdots & \vdots & \vdots \\ \gamma(\mathbf{x}_M, \mathbf{x}_1) & \gamma(\mathbf{x}_M, \mathbf{x}_2) & \cdots & 0 & 1 \\ 1 & 1 & \cdots & 1 & 0 \end{bmatrix} \tag{A5}$$

and

$$G_R = [\gamma(\mathbf{x}_1, \mathbf{x}_0)\ \gamma(\mathbf{x}_2, \mathbf{x}_0) \cdots 1]; \tag{A6}$$

where $\gamma(\mathbf{x}_i, \mathbf{x}_j) = \gamma(|\mathbf{x}_i - \mathbf{x}_j|)$ is the semivariance inferred from the semi-variogram model (i.e. the linear model fitting the binned observations in eq. (A1), not the observations themselves) and $\gamma(\mathbf{x}_i, \mathbf{x}_0)$ the semivariance (inferred from the same model) of the pairs 'observation point'–'interpolated point'.

SUPPORTING INFORMATION

Additional Supporting Information may be found in the online version of this article:

Figures S1–S2. Energy stacked and normalized in the five phases of the rupture process in the 0.4–3 Hz (Fig. S1) and 2–8 Hz band (Fig. S2).
Figures S3–S4. Histogram of number of aftershocks and of semblance maxima falling within 100 km either side of the trench-perpendicular transects together with the profiles of the cumulative energy for 0.4–3 Hz (Fig. S3) and 2–8 Hz (Fig. S4) results.
Figure S5. Difference between the static corrections with aftershocks (approach introduced here) and based on main shock hypocentre (standard procedure).
Figure S6. Progression of the semblance maxima for traveltimes without the dynamic corrections.
Figure S7. Spatial distribution of the cumulative energy for four aftershocks calculated with the approach proposed in this paper and the standard one.
Figure S8. Spatial distribution of the cumulative energy in the three frequency bands and along-strike projections (http://gji.oxfordjournals.org/lookup/suppl/doi:10.1093/gji/ggu311/-/DC1).

Please note: Oxford University Press is not responsible for the content or functionality of any supporting materials supplied by the authors. Any queries (other than missing material) should be directed to the corresponding author for the article.